AD-A072 403 GENERAL ELECTRIC CO SANTA BARBARA CA TEMPO F/G 15/6
SENSITIVITY OF HF BLACKOUT PREDICTIONS TO ATMOSPHERIC MINOR NEU--ETC(U)
MAY 79 R J JORDANO DAAD07-78-C-0005
UNCLASSIFIED GE79TMP-15 ERADCOM/ASL-CR-79-0005-1 NL

| OF |
AD
A072403

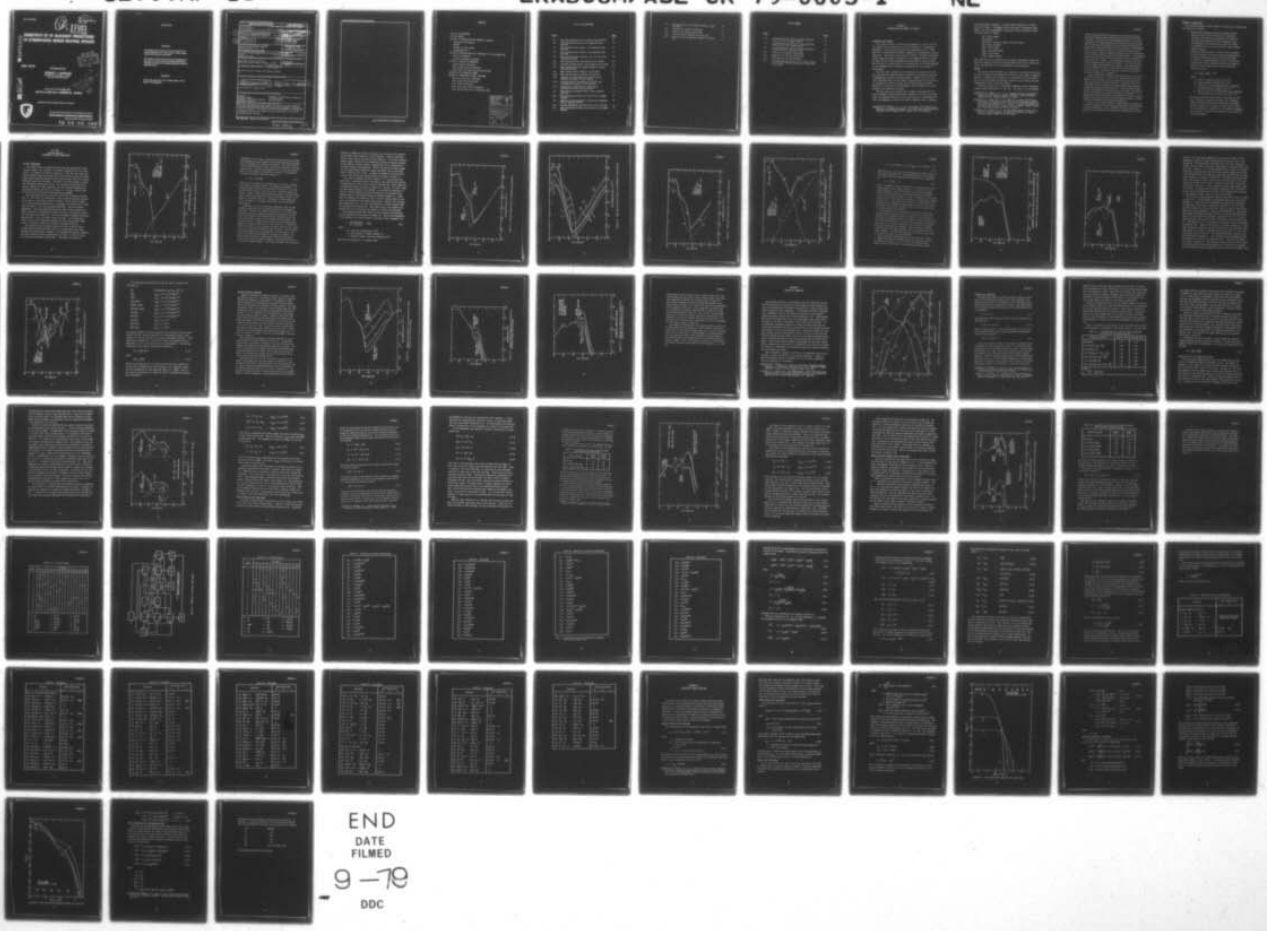

END
DATE
FILMED
9-79
DDC

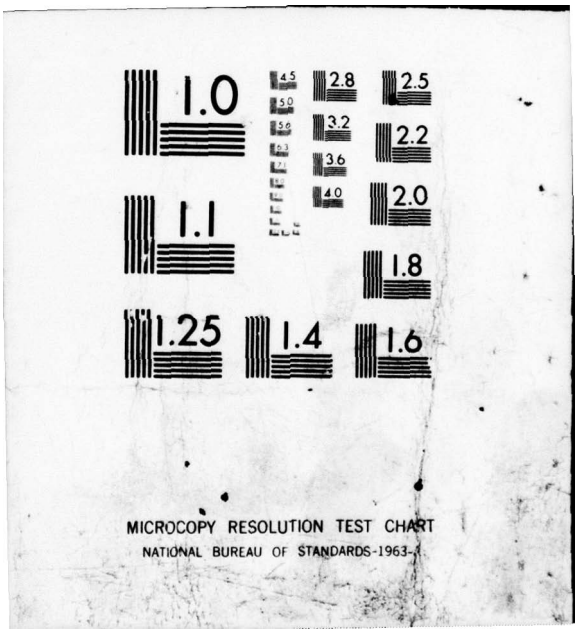
1.0
1.1
1.25
1.4
1.6
1.8
2.0
2.2
2.5
2.8
3.2
3.6
4.0
4.5
5.0
5.6
MICROCOPY RESOLUTION TEST CHART
NATIONAL BUREAU OF STANDARDS-1963-A

ASL-CR-79-0005-1

AD

Reports Control Symbol
OSD - 1366

12 LEVEL II

SENSITIVITY OF HF BLACKOUT PREDICTIONS TO ATMOSPHERIC MINOR NEUTRAL SPECIES

MAY 1979

Prepared by

ROBERT J. JORDANO
General Electric Company - TEMPO
Center for Advanced Studies

78 - per phone conversation with Shirley Rice - Procurement Office, TECOM, WSMR, NM. 8-25-78 - 3126 DELW ID

Under Contract DAADO7-85-C-0005
Contract Monitor: ROBERTO RUBIO

Approved for public release; distribution unlimited

US Army Electronics Research and Development Command
Atmospheric Sciences Laboratory
White Sands Missile Range, NM 88002

NOTICES

Disclaimers

The findings in this report are not to be construed as an official Department of the Army position, unless so designated by other authorized documents.

The citation of trade names and names of manufacturers in this report is not to be construed as official Government indorsement or approval of commercial products or services referenced herein.

Disposition

Destroy this report when it is no longer needed. Do not return it to the originator.

SECURITY CLASSIFICATION OF THIS PAGE (When Data Entered)

REPORT DOCUMENTATION PAGE

READ INSTRUCTIONS BEFORE COMPLETING FORM

1. REPORT NUMBER: ASL-CR-79-0005-1
2. GOVT ACCESSION NO.:
3. RECIPIENT'S CATALOG NUMBER:

4. TITLE (and Subtitle): SENSITIVITY OF HF BLACKOUT PREDICTIONS TO ATMOSPHERIC MINOR NEUTRAL SPECIES

5. TYPE OF REPORT & PERIOD COVERED: Final Report, 31 Oct 77 - 1 Nov 78

6. PERFORMING ORG. REPORT NUMBER: GE79TMP-15

7. AUTHOR(s): Robert J. Jordano

8. CONTRACT OR GRANT NUMBER(s): DAAD07-78-C-0005

9. PERFORMING ORGANIZATION NAME AND ADDRESS:
General Electric Company - TEMPO
816 State Street
Santa Barbara, California 93101

10. PROGRAM ELEMENT, PROJECT, TASK AREA & WORK UNIT NUMBERS: DA Task No. 1L162111AH71-A4

11. CONTROLLING OFFICE NAME AND ADDRESS:
US Army Electronics Research and Development Command
Adelphi, MD 20783

12. REPORT DATE: May 1979

13. NUMBER OF PAGES: 83

14. MONITORING AGENCY NAME & ADDRESS (if different from Controlling Office):
Atmospheric Sciences Laboratory
White Sands Missile Range, NM 88002

15. SECURITY CLASS. (of this report): UNCLASSIFIED

15a. DECLASSIFICATION/DOWNGRADING SCHEDULE:

16. DISTRIBUTION STATEMENT (of this Report):

Approved for public release; distribution unlimited

17. DISTRIBUTION STATEMENT (of the abstract entered in Block 20, if different from Report):

18. SUPPLEMENTARY NOTES:
ERADCOM/ASL

Contract Monitor: Roberto Rubio

19. KEY WORDS (Continue on reverse side if necessary and identify by block number):

Atmosphere
Atmospheric Models
Atmospheric Minor Neutral Species
Atmospheric Chemistry
Atmospheric Electromagnetic Propagation
HF Communications
Nuclear Blackout

20. ABSTRACT (Continue on reverse side if necessary and identify by block number):

This report presents most recent progress in a series of studies related to the sensitivity of HF wave absorption to atmospheric parameters. The sensitivity to atmospheric minor neutral species ~~(O, O_3, $O_2(a^1\Delta g)$, N, NO, NO_2, CO_2, and H_2O)~~ is presented, with emphasis on the recovery phase of an HF system following nuclear blackout.

DD FORM 1 JAN 73 1473 EDITION OF 1 NOV 65 IS OBSOLETE

SECURITY CLASSIFICATION OF THIS PAGE (When Data Entered)

346 420

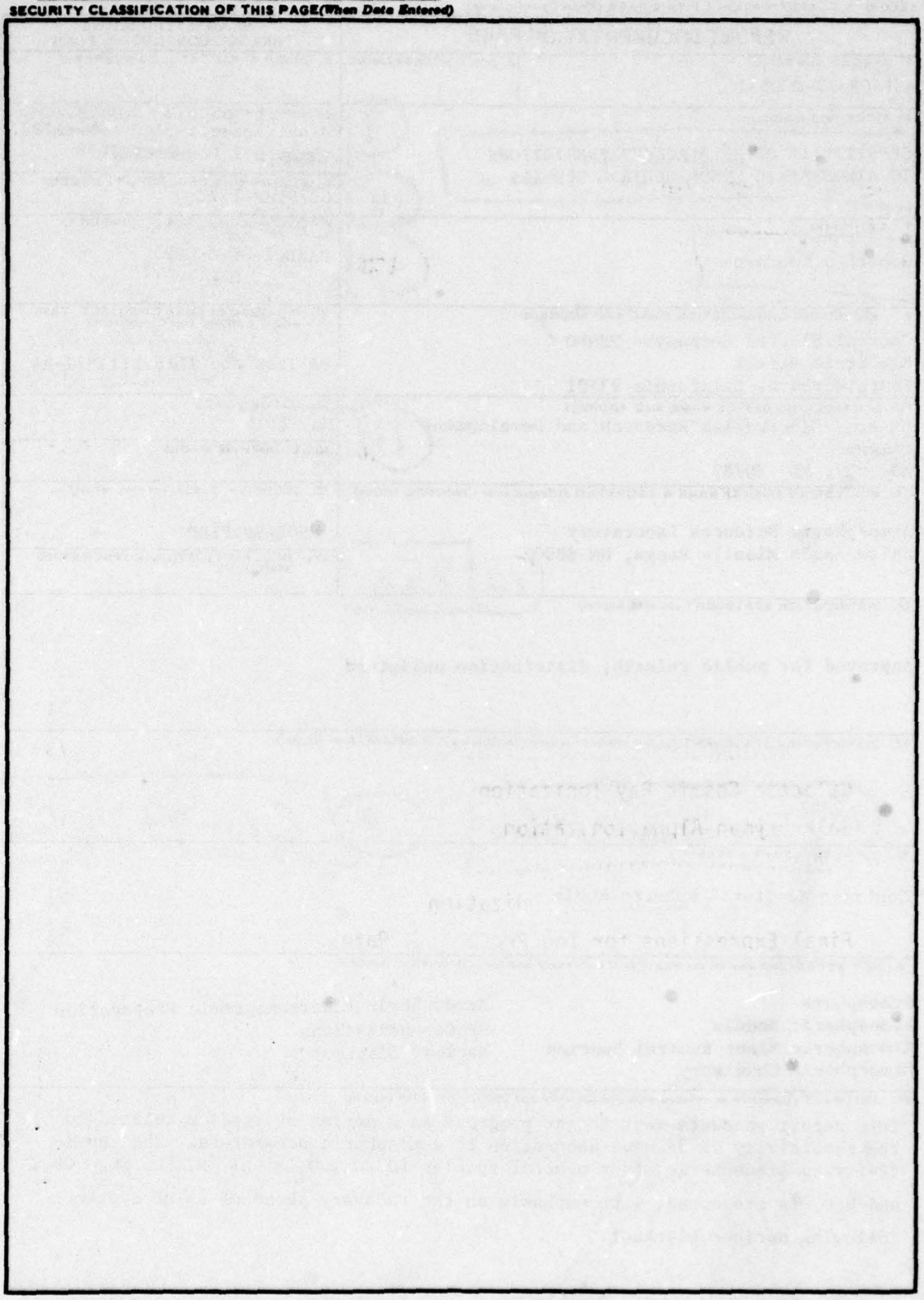

CONTENTS

LIST OF ILLUSTRATIONS

LIST OF TABLES

SECTION 1
INTRODUCTION AND SUMMARY OF RESULTS

BACKGROUND AND PURPOSE

This report presents our most recent progress in a series of studies related to the sensitivity of HF wave absorption to atmospheric parameters. The current effort has been supported by the U.S. Army Electronics Research and Development Command at the Atmospheric Sciences Laboratory. The purpose of the study is twofold. We hope to determine whether expected natural variations in the atmosphere should be incorporated into the various atmospheric nuclear effects computer models. We also expect to identify gaps or inconsistencies in the understanding of the atmosphere and to identify requirements for new atmospheric measurements.

The first report (Reference 1-1) addressed the sensitivity of HF wave absorption to expected natural variations in atmospheric profiles of temperature, pressure, and mass density. Exphasis was on the nuclear disturbed case, and the primary systems measure for the sensitivity analysis was circuit recovery time following nuclear blackout. Factors of 2 variation in wave absorption, and in duration of circuit blackout, were found to be typical.

The next step in the analysis was to address the sensitivity to minor atmospheric species variations. However, since little was known about the expected variations in the minor species, a preliminary effort was undertaken to collect and collate empirical data as reported

---

Reference 1-1. Jordano, R.J., et al, *Sensitivity of HF Blackout Predictions to Atmospheric Parameters (U)*, GE77TMP-16 (ARBRL-CR-00357), General Electric Company—TEMPO, August 1977 (Confidential).

in the technical literature. A second report (Reference 1-2) documents this effort. The emphasis was on the upper stratosphere, mesosphere, and lower thermosphere, where most HF wave absorption occurs. The minor species included

(O), atomic oxygen
(O_3), ozone
($O_2(a^1\Delta g)$), molecular oxygen, excited a-state
(N), atomic nitrogen
(NO), nitric oxide
(NO_2), nitrogen dioxide
(H_2O), water vapor
(CO_2), carbon dioxide.

Many other species are important to the general atmospheric model, but these are expected to have the primary *direct* effect on the ionization level, and therefore on the electromagnetic wave absorption.

METHOD

The present report documents our findings on the sensitivity of the HF wave absorption to the expected variations in these minor atmospheric species. A summary of conclusions is listed below, but first we present a brief description of the tools employed in the analysis and the organization of the rest of the report.

The basic analysis tool is the WEPH VI/ROSCOE D-region atmospheric chemistry model (References 1-3 and 1-4). The model is a considerable

Reference 1-2. Jordano, R.J., et al, *Suggested Natural Variations in Atmospheric Minor Neutral Species*, GE78TMP-26 (ARBRL-CR-00375), General Electric Company—TEMPO, July 1978.

Reference 1-3. Knapp, W.S., et al, *WEPH VI: A Fortran Code for the Calculation of Ionization and Electromagnetic Propagation Effects Due to Nuclear Detonations (U), Volume 3: Computational Models (U)*, GE75TMP-53 (DNA 3766T-3), General Electric Company—TEMPO, October 1976 (Confidential/Formerly Restricted Data).

Reference 1-4. Knapp, W.S., et al, *The ROSCOE Manual: Volume II: Atmospheric Chemistry Models*, GE74TMP-59 (DNA 3964F-11), General Electric Company—TEMPO (to be published).

simplification from the typical multi-species chemistry models that solve the coupled non-linear differential rate equations by numerical integration. The portion of the WEPH/ROSCOE model that we use is the steady-state ion species model which has shown particularly good agreement with the more detailed models in the altitude regime where HF absorption takes place (between 55 and 115 km altitude). The WEPH/ROSCOE model is of a form that is conducive to repetitive parametric sensitivity analyses. Hopefully, important conclusions can be verified with the more detailed (and more expensive) numerical models. The WEPH/ROSCOE model accepts the neutral species concentrations, and the various ion production rates, as inputs. It then computes steady-state concentrations of electrons and a few dozen ion species. For the levels of nuclear disturbance investigated in this analysis, the energy deposition rates are sufficiently small that the neutral species concentrations are not disturbed. The species, reactions, and method of solution of the model are summarized in Appendix A.

A second analysis tool employed in the present study is the natural ion production rate model. The solar flux impinging on top of the atmosphere and the interaction cross-sections with the air species are complicated functions of photon wavelength. Computation of the solar ion production rate at any point in the atmosphere requires numerical integrations over these spectral functions. We have assembled simple analytic representations of the natural solar and cosmic ion production rates in which much of the spectral integration is precomputed. The formulations do retain the necessary functional relationships to reflect proper sensitivity to variations in the atmospheric parameters, however. These model formulations are presented in Appendix B.

Section 2 of this report presents a general analysis of atmospheric HF wave absorption, both in the natural ionosphere and under conditions of nuclear disturbance. This is intended as a general orientation, in preparation for the sensitivity analysis which is presented in Section 3.

SUMMARY OF CONCLUSIONS

This section presents a brief summary of conclusions obtained from the sensitivity analysis

- Daytime high-frequency radiowave absorption occurs between 55 and 115 km in the natural ionosphere. Typically two-thirds of the absorption is caused by the Lyman-alpha radiation in the mesosphere, with the remainder distributed between cosmic ray (upper stratosphere) and x-ray and ultraviolet (lower thermosphere) sources.
- During the recovery phase of an HF circuit following nuclear blackout, the nuclear enhanced absorption due to delayed radiations occurs below 80 km altitude.
- In terms of a lumped-parameter solution, the electron concentration may be represented by the following expression in the regions where significant HF wave absorption occurs:

$$(e) \cong \frac{D}{D+A}\sqrt{q/\alpha_d} \quad cm^{-3}$$

where

q = total ion production rate ($cm^{-3}\ s^{-1}$)

A = total electron attachment rate (s^{-1})

D = effective electron detachment rate, depending on distribution of negative ions (s^{-1})

α_d = effective electron recombination rate, depending on distribution of positive ions ($cm^{-3}\ s^{-1}$).

- Increasing the minor oxygen species concentrations (O), (O_3), ($O_2(a^1\Delta g)$), generally increases the integrated vertical one-way HF absorption through the atmosphere. Species variations of a factor of 9 give about a factor of 1.25 variation in absorption in the natural ionosphere, and typically a factor of 2 variation in the nuclear disturbed ionosphere.

- Variation of the oxygen species has impact generally through the detachment rate D. Both (O) and ($O_2(a^1\Delta g)$) enhance the detachment rates for O_2^- and O^-. Increasing (O) also tends to increase the relative proportions of (O_2^-) and (O^-), while increasing (O_3) and ($O_2(a^1\Delta g)$) has the reverse effect. Thus (O) is the most important minor oxygen species.
- Increasing the minor nitrogen species concentrations (N), (NO), (NO_2) generally increases the integrated vertical one-way HF wave absorption through the atmosphere. Species variation of a factor of 9 give about a factor of 2 variation in absorption in the natural ionosphere, and typically less than a factor of 1.1 variation in the nuclear disturbed ionosphere.
- The most important nitrogen species is (NO) which acts primarily through the (Lyman-alpha) ion production rate q.
- Increasing (CO_2) and (H_2O) generally decreases the integrated vertical one-way HF wave absorption through the atmosphere. Species variations of a factor of 9 give only a factor of 1.1 to 1.2 variation in the absorption, acting mainly through α_d.

RECOMMENDATIONS

The important species identified are (O), (O_3), ($O_2(a^1\Delta g)$), and (NO), with the oxygen species being most important under nuclear disturbed conditions and the nitric oxide being most important under natural conditions. Variations of an order of magnitude in the daytime concentrations of these species are certainly possible as a function of latitude and season. This could yield a factor of 2 variation in the integrated one-way vertical HF wave absorption. This is comparable to the potential variations due to changes in temperature, pressure, and mass density that were observed in an eralier study. These variations are important to the prediction of HF circuit recovery following

nuclear blackout and the variable atmospheres should be incorporated into the nuclear effects computer models. Additional atmospheric measurements are required to expand and verify our understanding of the minor species variations, particularly at mesospheric altitudes.

SECTION 2

BASELINE ANALYSIS
ATMOSPHERIC HF WAVE ABSORPTION

NATURAL IONOSPHERE

The total natural ion production rate for mean conditions at noon (sunspot number = 60, latitude = 45 degrees, spring/fall season, solar zenith = 45 degrees) is shown in Figure 2-1. Note that the cosmic ray source dominates from the surface up to about 65 km altitude, the Lyman-alpha source dominates between 65 and 95 km altitude, and the UV source dominates above 95 km altitude. The solar x-ray source makes a secondary contribution above about 90 km. The production rate profile, of course, changes for other conditions, but the essential character of the profile remains the same as in Figure 2-1. We shall discuss each of the kinds of variations in the following paragraphs.

The variations with solar activity are easy to visualize from Figure 2-1. The cosmic ray source has a total variation of about a factor of 3: that is, an increase of about a factor 1.5 over that in Figure 2-1 for solar minimum conditions, or a decrease of a factor of 0.5 from that in Figure 2-1 for solar maximum conditions. Note the inverse dependence. The Lyman-alpha and UV sources show a total variation of about a factor of 2 (decreasing a factor of 0.67 or increasing a factor of 1.33 from that in Figure 2-1, for solar minimum or maximum conditions, respectively). The x-ray source varies the most. It may decrease a factor of 10 or more from that in Figure 2-1 for solar minimum conditions, or increase a factor of 2 for solar maximum conditions.

The variations with latitude, season, and time of day all have a strong variation characterized by the solar zenith angle, plus some secondary variations due to changes in the atmospheric pressure, density, and major and minor species concentration profiles. We shall discuss the variations with solar zenith first. The cosmic ray source is

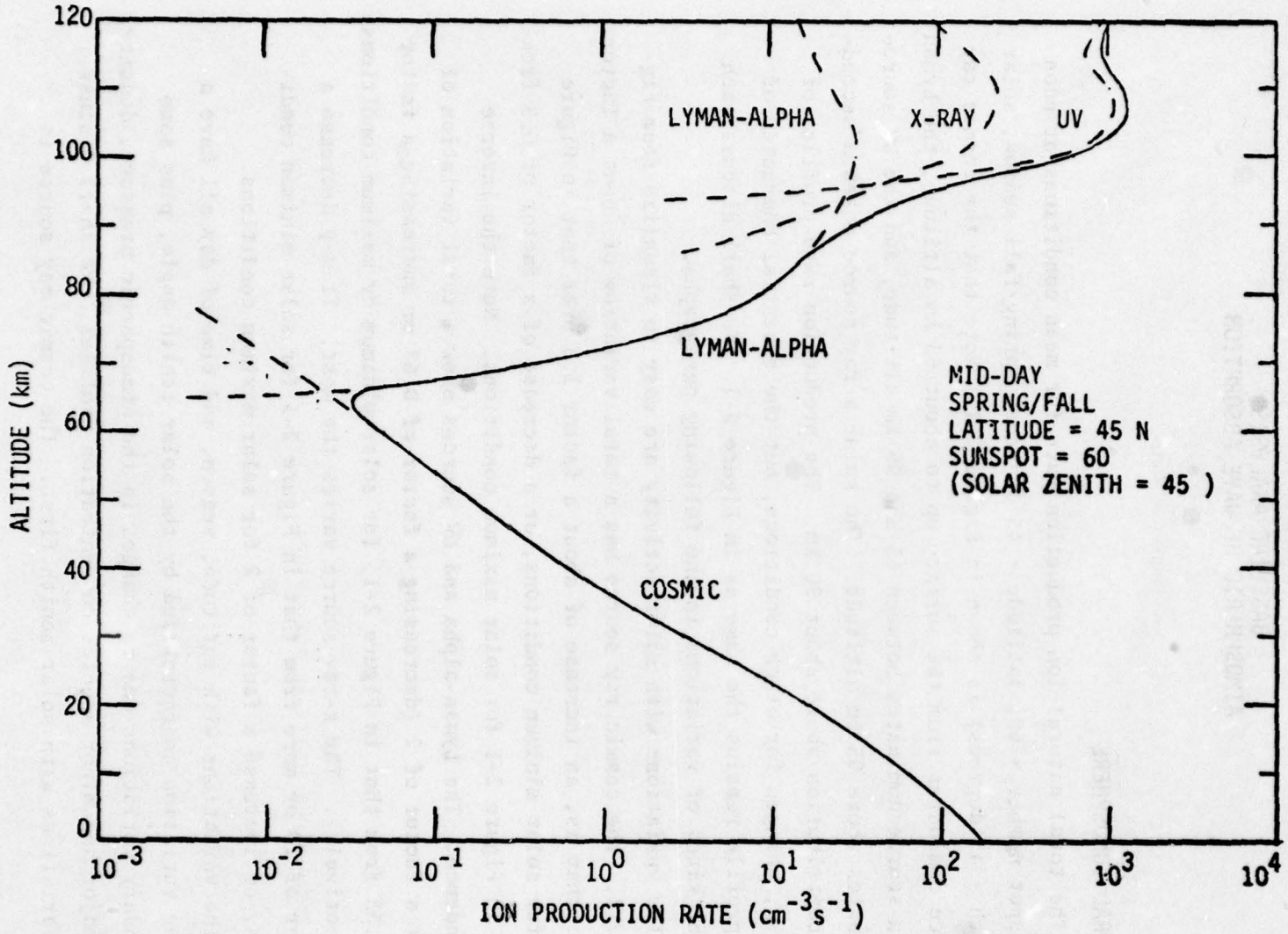

Figure 2-1. Mean daytime natural ion production rate profile.

independent of solar zenith. Each of the other sources has the zenith angle dependence in the attenuation function which determines how deep into the atmosphere the radiation can penetrate. Thus, the variation in solar zenith effectively raises or lowers the underside of the given source profile. From the secχ dependence, one can show that the altitude for a given number of attenuation e-foldings, or the effective altitude of the profile underside, varies as

$$h = h_0 - H_s \ln(\cos\chi) \qquad (2\text{-}1)$$

where h_0 is the altitude for an overhead sun (χ=0), and H_s = pressure scale height (e-folding distance). The pressure scale height in the underside regions (60-85 km for Lyman-alpha, 80-100 km for x-ray, and 90-100 km for UV sources) is about 6 to 7 km. Thus for example, the effective height of each of these profiles in Figure 2-1 may be lowered about 2 km for an overhead sun, or may be raised about 2 km for χ = 60 degrees, raised about 6 km for χ = 75 degrees, or raised about 9 km for χ = 80 degrees. (For higher zenith angles the secχ dependence breaks down.)

In addition to the solar zenith angle dependence, there are some secondary variations in the ion production rate due to atmospheric variations. The cosmic ray source is proportional to the total number density which can have seasonal variations of 10 percent at mid-latitudes, and 40 percent at the higher latitudes (the densities are low in winter and high in summer in the important altitude regime). The Lyman-alpha source is proportional to the nitric oxide concentrations. Seasonal variations of (NO) of plus or minus a factor of 2 (maximum in summer) are expected at mid-latitudes, and higher concentrations (factor of 4) at all seasons are expected at higher latitudes. The attenuation of the Lyman-alpha source is determined by the line integral of (O_2) penetrated, which varies approximately like the local pressure. At the altitudes of interest to Lyman-alpha attenuation, the pressure varies about 10 percent (maximum in summer) at mid-latitudes and about 40 percent at higher latitudes. At the higher latitudes, this effectively

raises (in summer) or lowers (in winter) the altitude of the underside of the Lyman-alpha profile by a few kilometers. Similar variations will be seen in the x-ray and UV source profiles. In the 90 to 100 km region, these profiles will be effectively raised or lowered slightly, in the summer or winter seasons, respectively, due to variations in the major species concentrations. The UV ionization of atomic oxygen will be significantly reduced at higher latitudes, due to the lower levels (factor of 10) of (O). A couple of examples of natural variations in the daytime ion production rate are shown in Figure 2-2.

The total ion production rate of Figure 2-1 is partitioned into particular ion production rates according to the prescriptions defined in Equations B-4, B-24 to B-26, and B-31 through B-35. These *phase one* ion production rates are shown in Figure 2-3. The N_2^+, N^+, and O^+ undergo rapid charge transfer to O_2^+ and NO^+, as described in Equations A-1 and A-2, and the effective O_2^+ and NO^+ *phase two* ion production rate profiles used in the chemistry model are shown in Figure 2-4. Note that the dominant ion production rate is for NO^+ between about 65 and 95 km, due primarily to the Lyman-alpha source. Below 65 km, the dominant production rate is for O_2^+, due primarily to charge transfer from the N_2^+ produced by cosmic rays. Above about 95 km, the dominant production rate is also for O_2^+, due primarily to direct UV ionization.

The resulting steady-state total ion and electron concentrations for this daytime case are shown in Figure 2-5. The HF wave absorption is due primarily to electron-neutral collisions, and is computed from

$$a = \frac{4.6 \times 10^4 \, (e)\nu}{\omega^2 + (0.775\nu)^2} \quad \text{dB/km} \qquad (2\text{-}2)$$

where

(e) = electron concentration (cm^{-3})

ω = wave carrier frequency (radian s^{-1})

ν = electron neutral collision frequency (s^{-1}).

The collision frequency ν is computed from

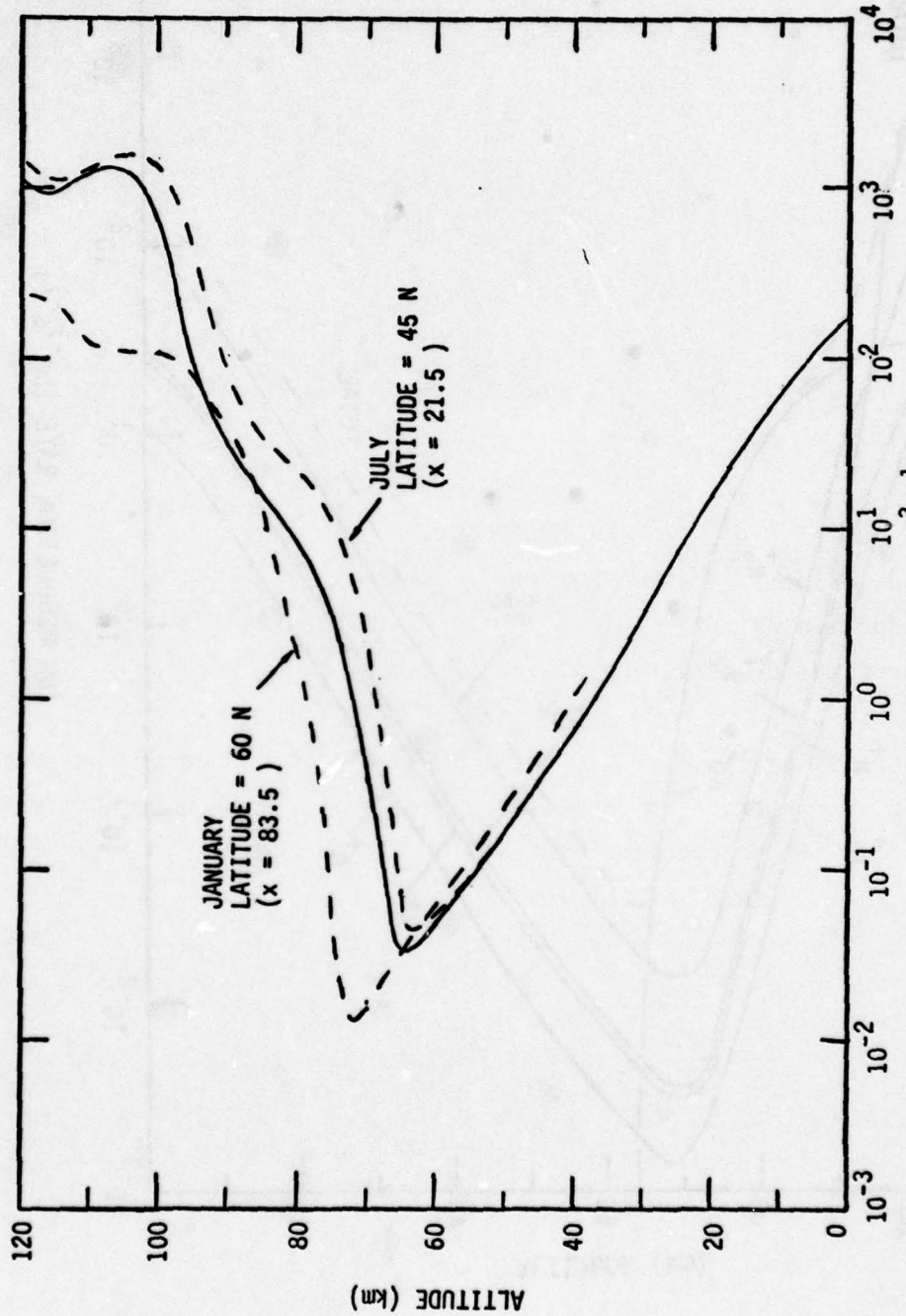

Figure 2-2. Alternate daytime natural ion production rate profiles.

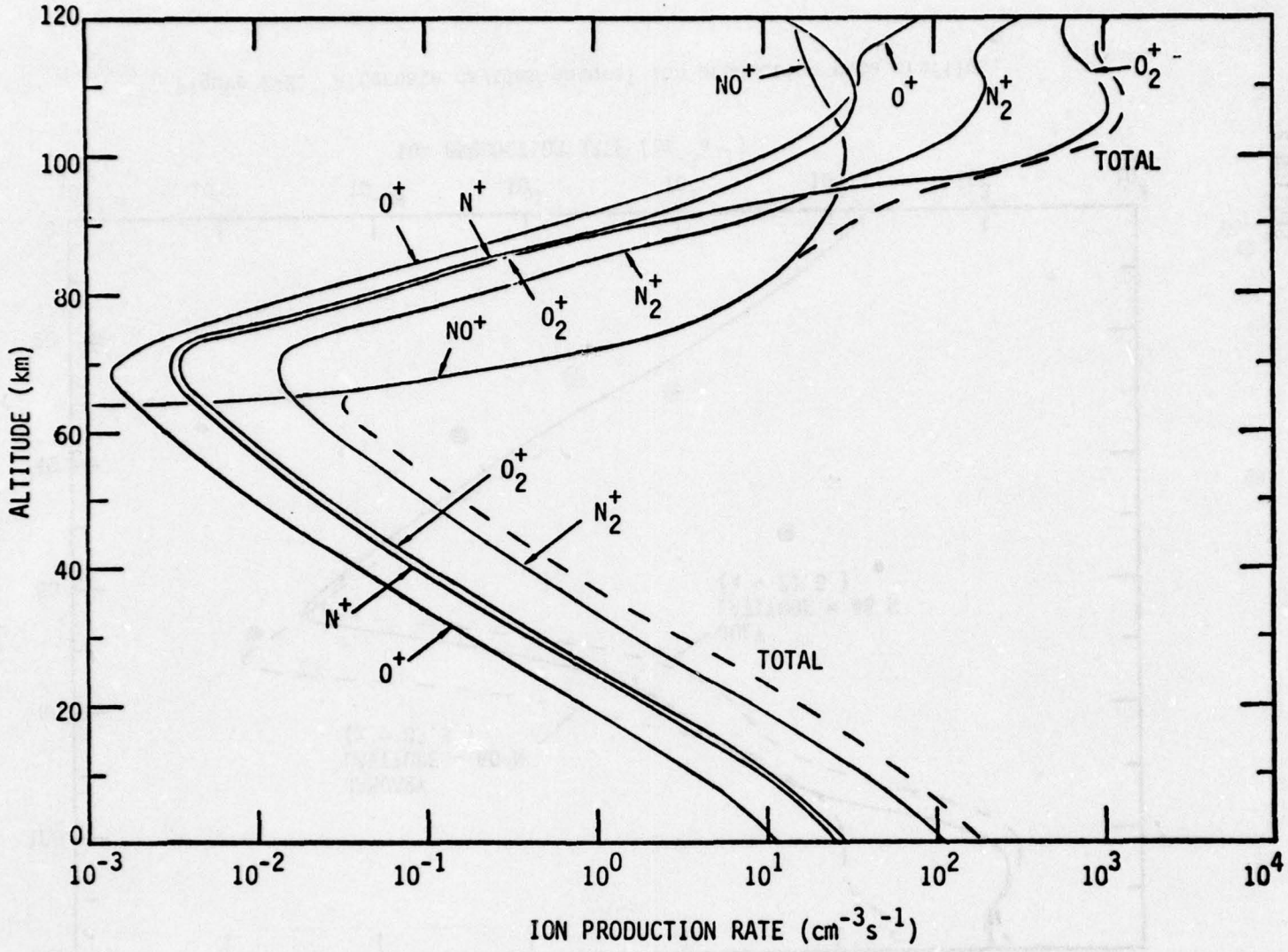

Figure 2-3. Mean daytime natural phase 1 ion production rate profiles.

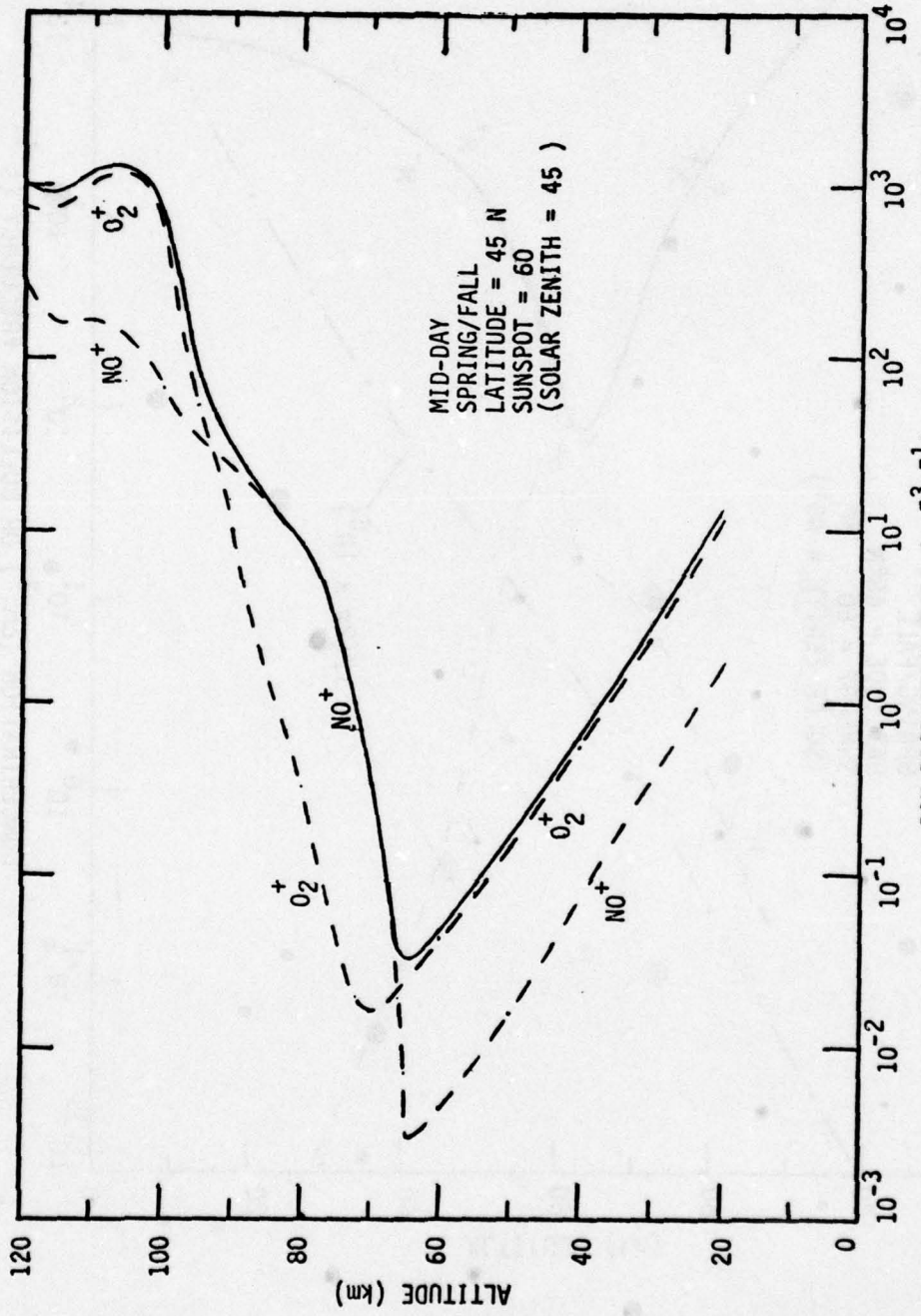

Figure 2-4. Mean daytime natural phase 2 ion production rate profiles.

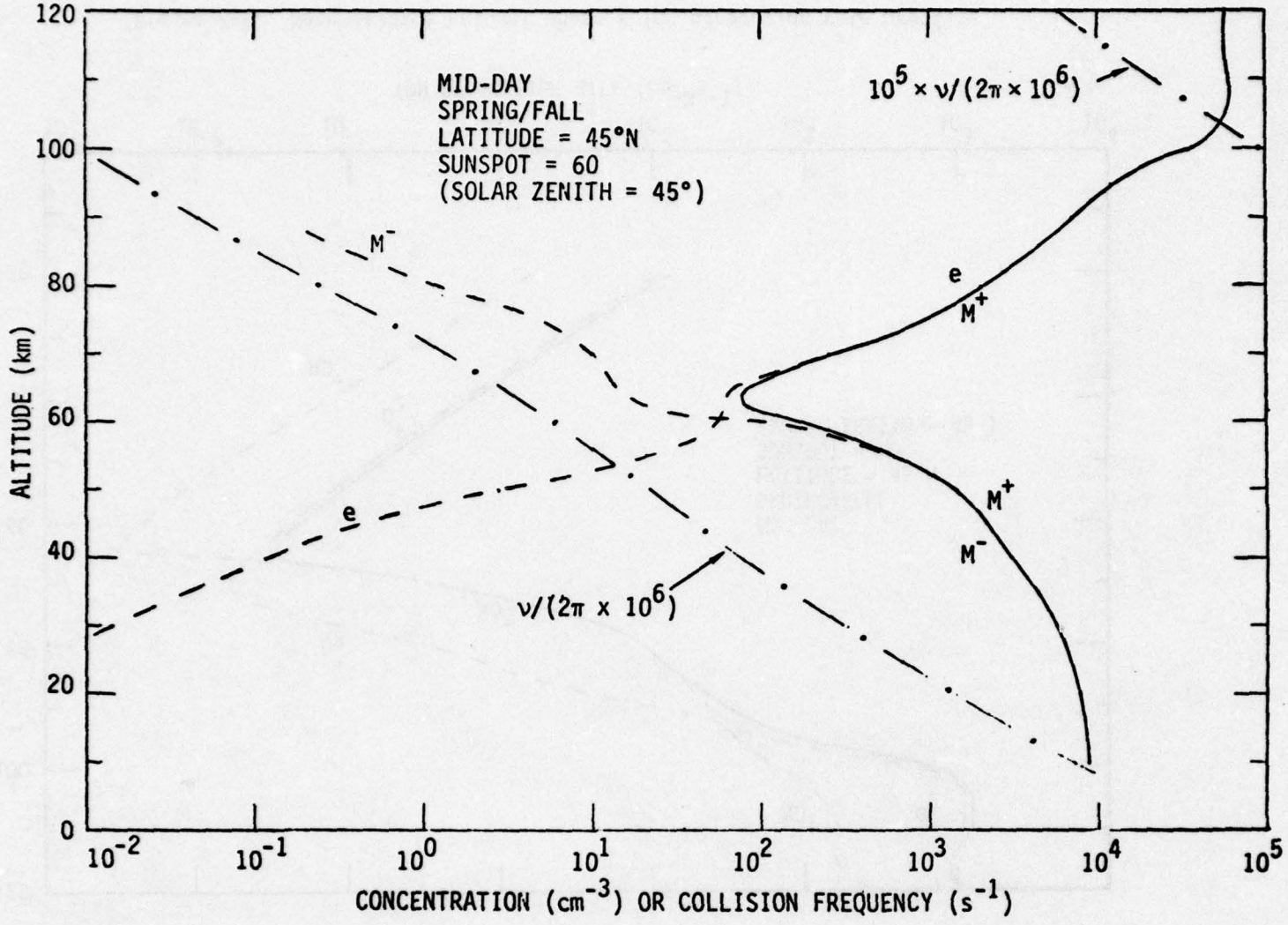

Figure 2-5. Mean daytime natural electron, ion, and collision frequency profiles.

$$\nu = 2.6 \times 10^{-11}(N_2)T + 1.5 \times 10^{-11}(O_2)T + 8.2 \times 10^{-10}(O)T^{\frac{1}{2}} \quad s^{-1} \tag{2-3}$$

where (N_2), (O_2), and (O) are species concentrations (cm^{-3}), and T is the electron temperature (K). Note that below about 90 km altitude, the third term may be neglected and the expression for ν simplifies to

$$\nu = 1.7 \times 10^{5} P \quad s^{-1} \tag{2-4}$$

where P = atmospheric pressure (dyne cm^{-2}). The electron neutral collision frequency is also shown in Figure 2-5. Note that the actual quantity plotted is $\nu/(2\pi \times 10^{6})$ which gives the collision frequency in units directly comparable to the carrier frequency in megahertz. Thus for an HF carrier frequency of 10 MHz, for example, ω is less than ν below about 55 km altitude and the absorption is approximately proportional to $(e)/\nu$. Above about 55 km altitude, ω is greater than ν and the absorption is approximately proportional to $(e)\nu/\omega^{2}$. For the typical HF band, this crossover altitude is seen to vary from about 65 km (for 3 MHz) to about 45 km (30 MHz).

The incremental and cumulative (one-way vertical) absorption for a 10 MHz signal are shown in Figure 2-6. Note that 99 percent of the absorption occurs between 55 and 115 km altitude. The three *bumps* in the incremental absorption profile correspond to regions where different ionization sources dominate. The bulk of the absorption (about 60 percent) occurs in the central bump between about 70 and 95 km altitude, where the Lyman-alpha source dominates. About 25 percent of the absorption occurs in the upper bump above 95 km, where the UV and x-ray sources dominate. Only about 15 percent of the absorption occurs below 65 km, where the cosmic ray source dominates.

These observations change somewhat for other conditions. Figure 2-7 compares incremental absorption profiles for the alternate ionization profiles of Figure 2-2. In all cases, the absorption occurs between 55 and 115 km altitude. For the midlatitude summer profile,

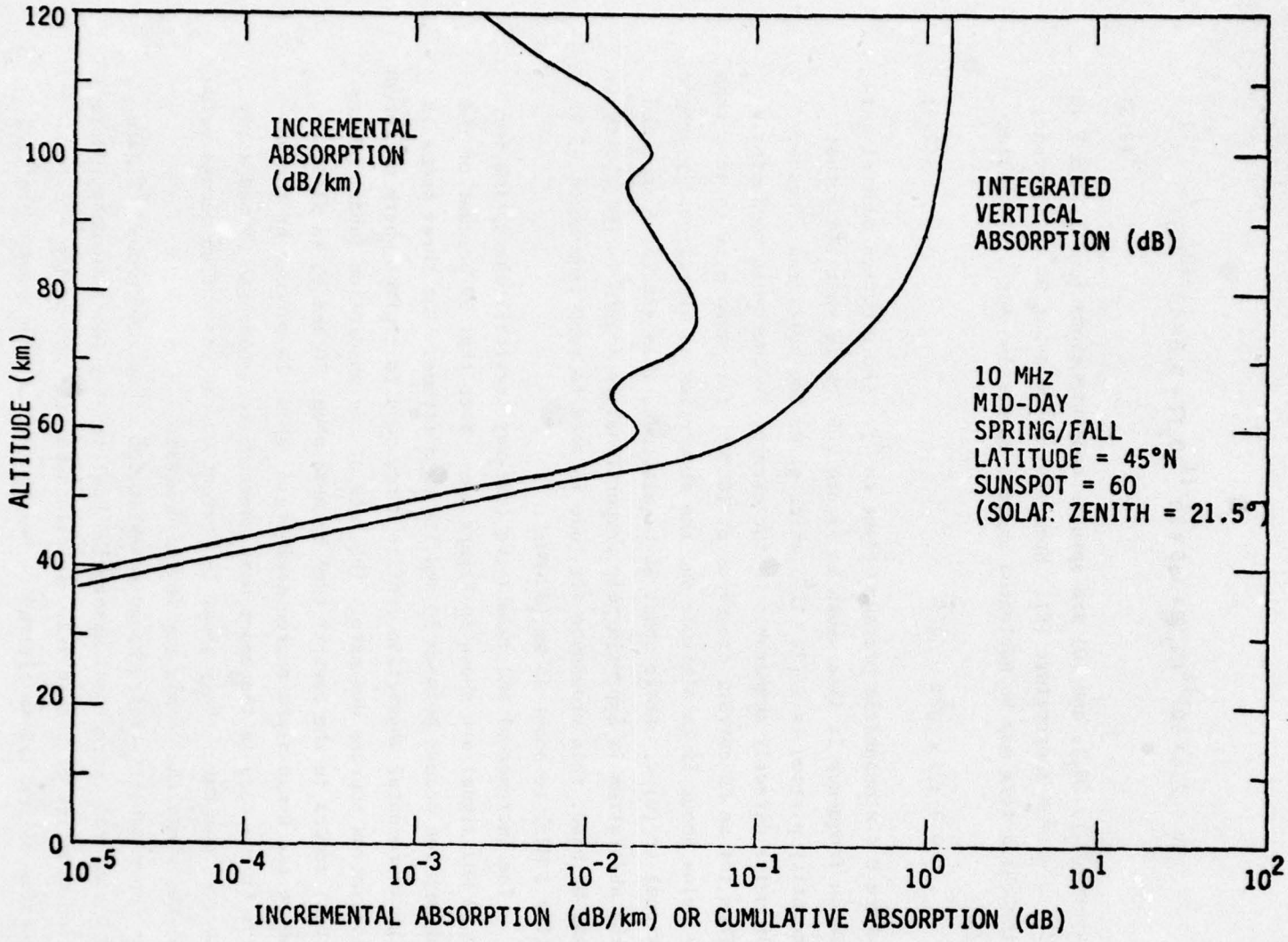

Figure 2-6. Mean daytime natural wave absorption at 10 MHz.

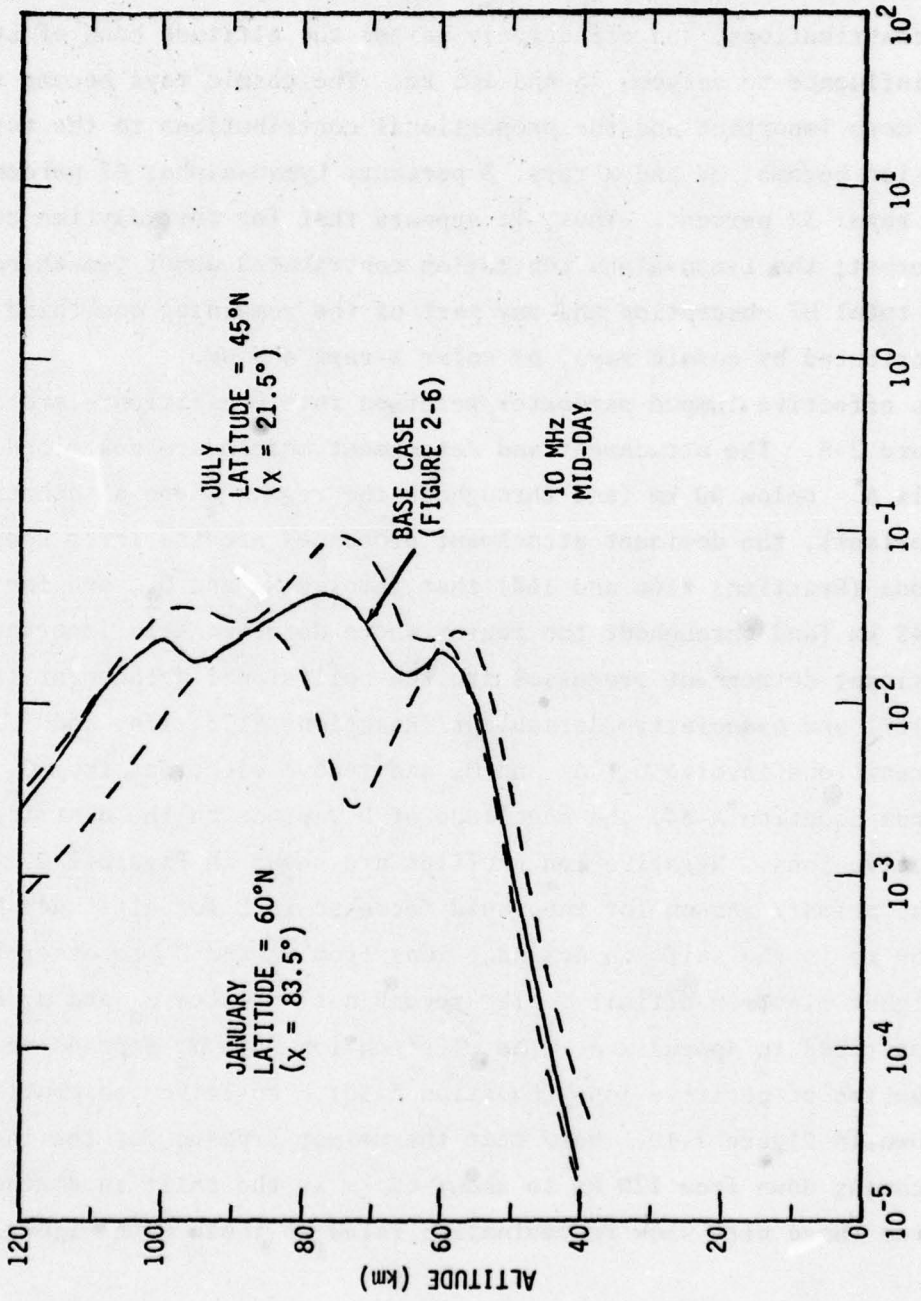

Figure 2-7. Alternate daytime natural wave absorption at 10 MHz.

the UV, x-ray, and Lyman-alpha energy all penetrate deeper into the atmosphere, tending to swamp the contribution of cosmic rays to the absorption. The proportional contributions to the total absorption become: UV and x-rays: 34 percent; Lyman-alpha: 66 percent; cosmic rays: less than 1 percent. For the high-latitude winter profile, the larger atmospheric attenuation of the solar flux severely reduces the UV and x-ray contributions, and effectively raises the altitude band of Lyman-alpha influence to between 75 and 105 km. The cosmic rays become relatively more important and the proportional contributions to the total absorption become: UV and x-rays: 3 percent; Lyman-alpha: 65 percent; cosmic rays: 32 percent. Thus, it appears that for most daytime cases of interest, the Lyman-alpha ionization contributes about two-thirds of the total HF absorption and any part of the remaining one-third may be contributed by cosmic rays, or solar x-rays and UV.

The effective lumped-parameter reaction rate coefficients are shown in Figure 2-8. The attachment and detachment models are described in Appendix A. Below 90 km (and throughout the region where attachment is important), the dominant attachment processes are the three body reactions (Reactions #166 and 168) that involve N_2 and O_2, and form O_2^-. Above 45 km (and throughout the region where detachment is important), the dominant detachment processes are the collisional detachment (Reaction #177) and associative detachment (Reactions #173, 174, and 176). These reactions involve $O_2(^1\Delta)$ and O, and remove electrons from O_2^- and O^-. From Equation A-34, the magnitude of D depends on the distribution of negative ions. Negative ion profiles are shown in Figure 2-9. Note that the primary reason for the rapid decrease in D for altitudes below about 60 km is the shift in dominant ions from O_2^- and O^- to other ions with higher electron affinity. The recombination rates α_d and α_i are also described in Appendix A. The electron-ion rate α_d depends on the distribution of positive ions (Equation A-33). Positive ion profiles are shown in Figure 2-10. Note that the primary reason for the increase in α_d coming down from 120 km to about 60 km is the shift in dominant ions from those with slow recombination rates to those with higher rates.

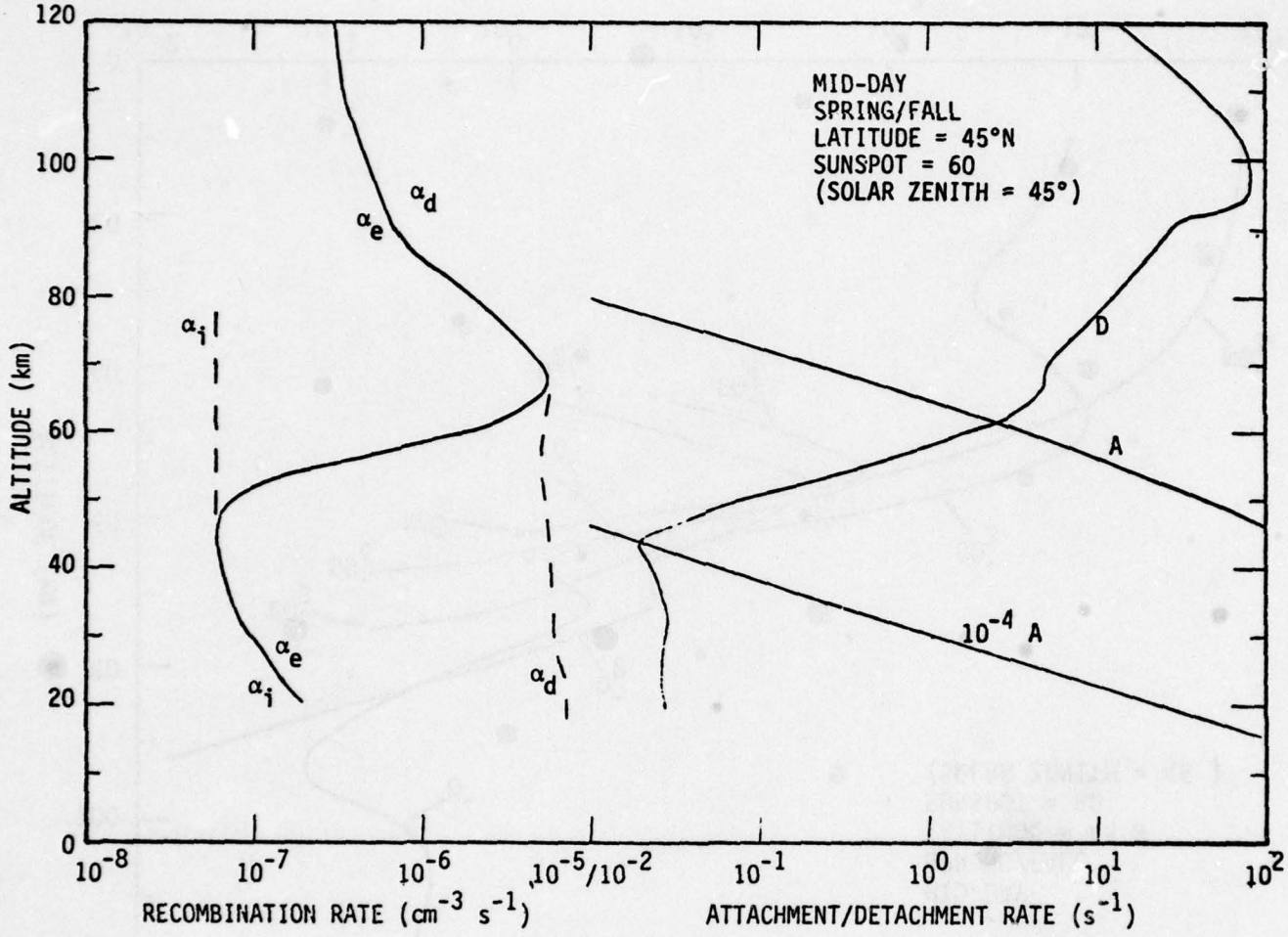

Figure 2-8. Mean daytime effective lumped parameter reaction rate coefficients.

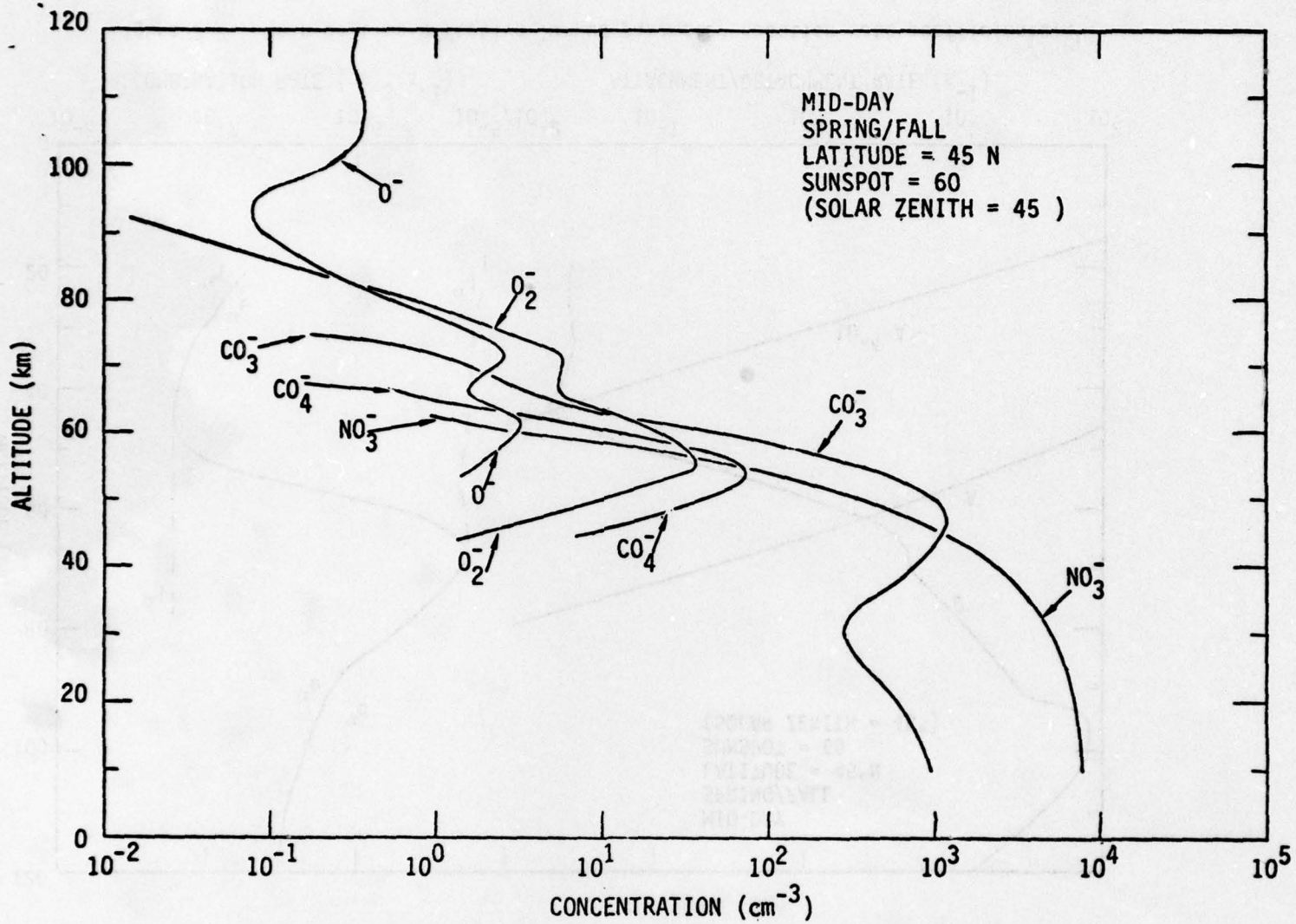

Figure 2-9. Mean daytime natural negative ion profiles.

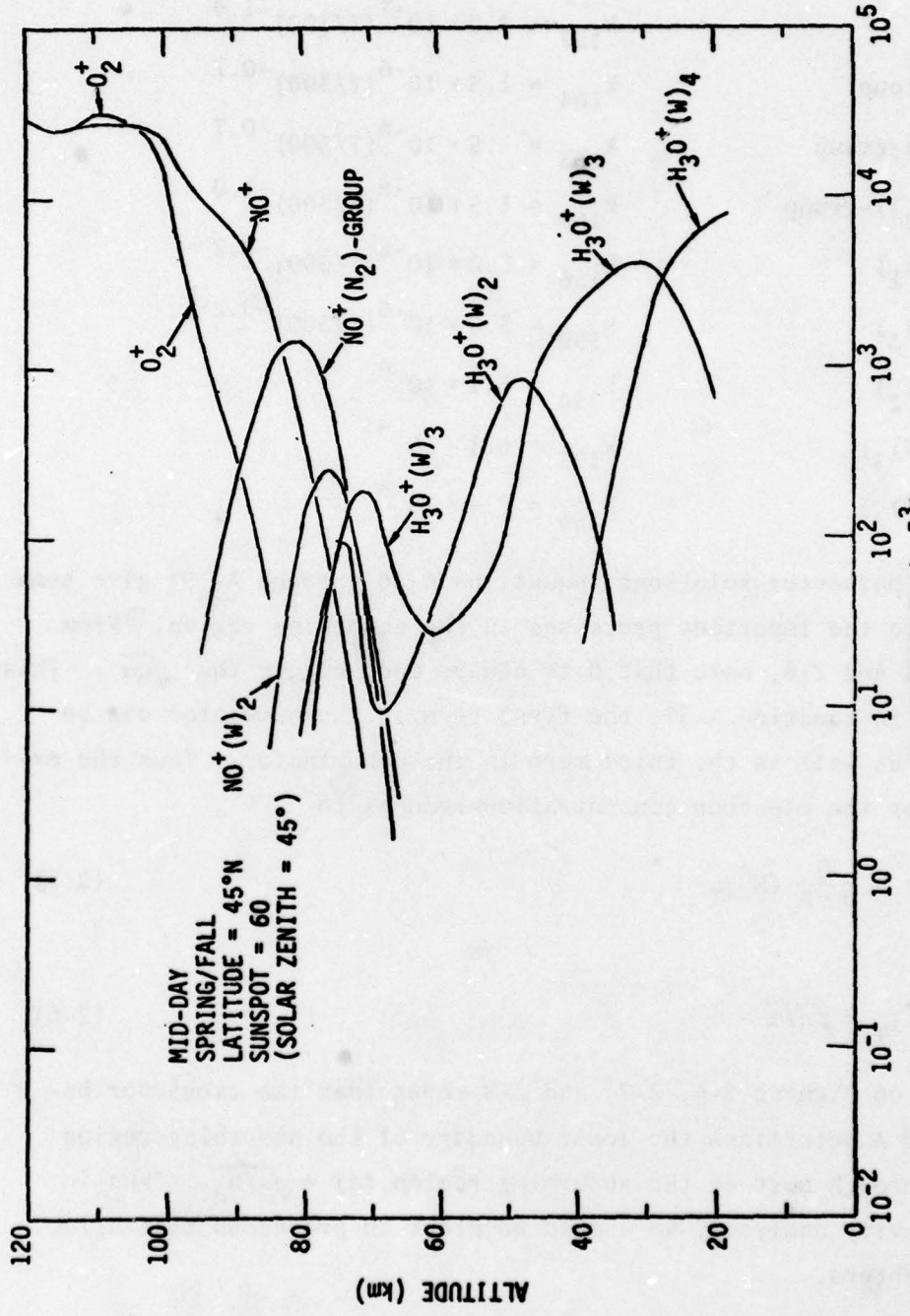

Figure 2-10. Mean daytime natural positive ion profiles.

The following list presents the ions and rates in order of increasing α_d:

Ion	Recombination rate α_d ($cm^3\ s^{-1}$)
(O_2^+)	$k_{162} = 2.1 \times 10^{-7}(T/300)^{-0.7}$
(NO^+)	$k_{157} = 4.0 \times 10^{-7}(T/300)^{-1.0}$
(O_4^+)-group	$k_{164} = 1.5 \times 10^{-6}(T/300)^{-0.7}$
$(O_2^+(W))$-group	$k_{163} = 2.5 \times 10^{-6}(T/300)^{-0.7}$
$(NO^+(N_2))$-group	$k_{160} = 1.5 \times 10^{-6}(T/300)^{-1.0}$
$(NO^+(W)_2)$	$k_{158} = 3.0 \times 10^{-6}(T/300)^{-0.2}$
$(NO^+(W)_3)$	$k_{159} = 5.0 \times 10^{-6}(T/300)^{-0.2}$
$(H_3O(W)_2)$	$k_{154} = 5.1 \times 10^{-6}$
$(H_3O)(W)_3)$	$k_{155} = 6.1 \times 10^{-6}$
$(H_3O^+(W)_4)$	$k_{156} = 7.4 \times 10^{-6}$

The lumped-parameter solutions (Equations A-36 through A-39) give some insight into the important processes in the absorbing region. From Figures 2-1 and 2-8, note that D is always much bigger than $\sqrt{q\alpha}$. This means that in Equation A-37, the first term in the numerator can be neglected, as well as the third term in the denominator. Thus the expression for the electron concentration reduces to

$$(e) = \frac{D}{D + A}\,(M^+)_T \qquad (2\text{-}5)$$

where

$$(M^+)_T = \sqrt{q/\alpha} \quad . \qquad (2\text{-}6)$$

Reflection on Figures 2-6, 2-7, and 2-8 shows that the crossover between D and A determines the lower boundary of the absorbing region and that through most of the absorbing region $(e) = \sqrt{q/\alpha_d}$. Thus in the sensitivity analyses, we should be alert to processes that affect these parameters.

NUCLEAR DISTURBED IONOSPHERE

Examples of enhanced ion production rate due to a nuclear source are shown in Figure 2-11. The nuclear source is gamma-ray energy deposition from radioactive fission debris. The sequence of curves (those labeled A, B, C) represent the relaxation of the disturbance due to the time decay of the radioactive fission products. Each curve represents a factor of 10 reduction in nuclear energy deposition from the previous curve. Since the decay of the gamma-ray energy output follows a $(1 + t)^{-1.2}$ behavior (t is time after burst), the sequence of curves represent factors of about 7 increase in time after burst. These curves could represent relatively fresh fission debris from a small yield burst or one which is very distant: in this case the time intervals between curves A, B, and C would be relatively short (eg, A = 9 s, B = 1 min, C = 7 min). The curves could also be matched by much older fission debris from a larger burst or one nearby: in this case the time interval between curves could be much longer (eg, A = 7 min, B = 50 min, C = 6 hours). The curve labeled NATURAL is the same as that in Figure 2-1.

The corresponding enhancement of electron concentrations and HF wave absorption are shown in Figures 2-12 and 2-13. The important thing to notice in Figures 2-11 through 2-13 is that the nuclear disturbance only affects the ionosphere below about 80 km altitude. This result is representative of levels of disturbance encountered during the recovery phase of an HF system. The tic marks on the curves in Figure 2-12 delineate the altitude interval where 90 percent of the total vertical integrated absorption occurs.

From Equations 2-5 and 2-6, the electron and total positive ion density (and therefore also the total negative ion density) are approximately proportional to the square root of the ion production rate q. Variation from this dependence would arise only from a change in the effective reaction rates A, D, α, or α_d as a function of q. Comparison of Figures 2-10 and 2-11 shows that the square-root dependence holds to a close approximation. Careful examination of the calculated

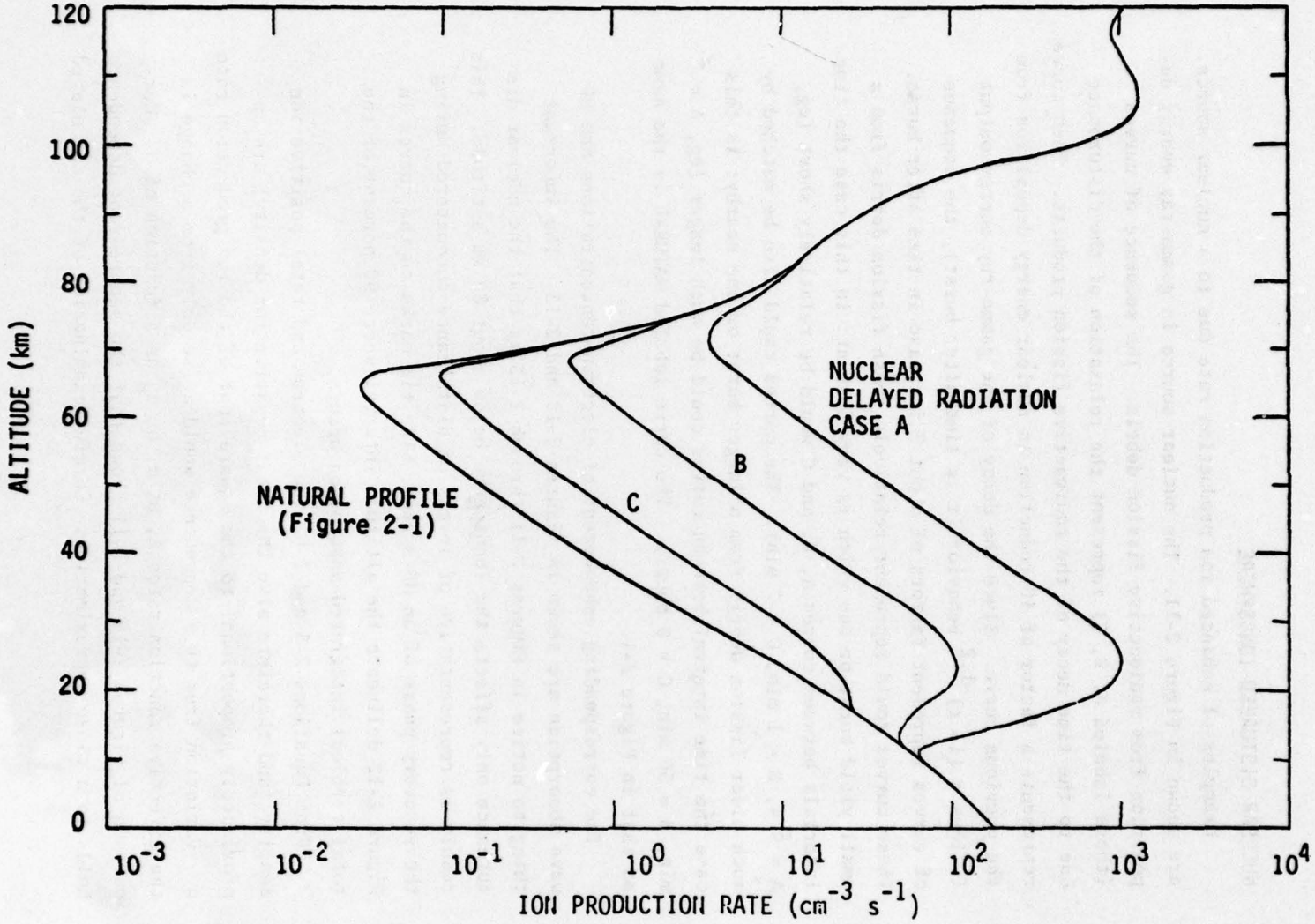

Figure 2-11. Enhanced ion production rate profiles due to radioactive nuclear fission sources.

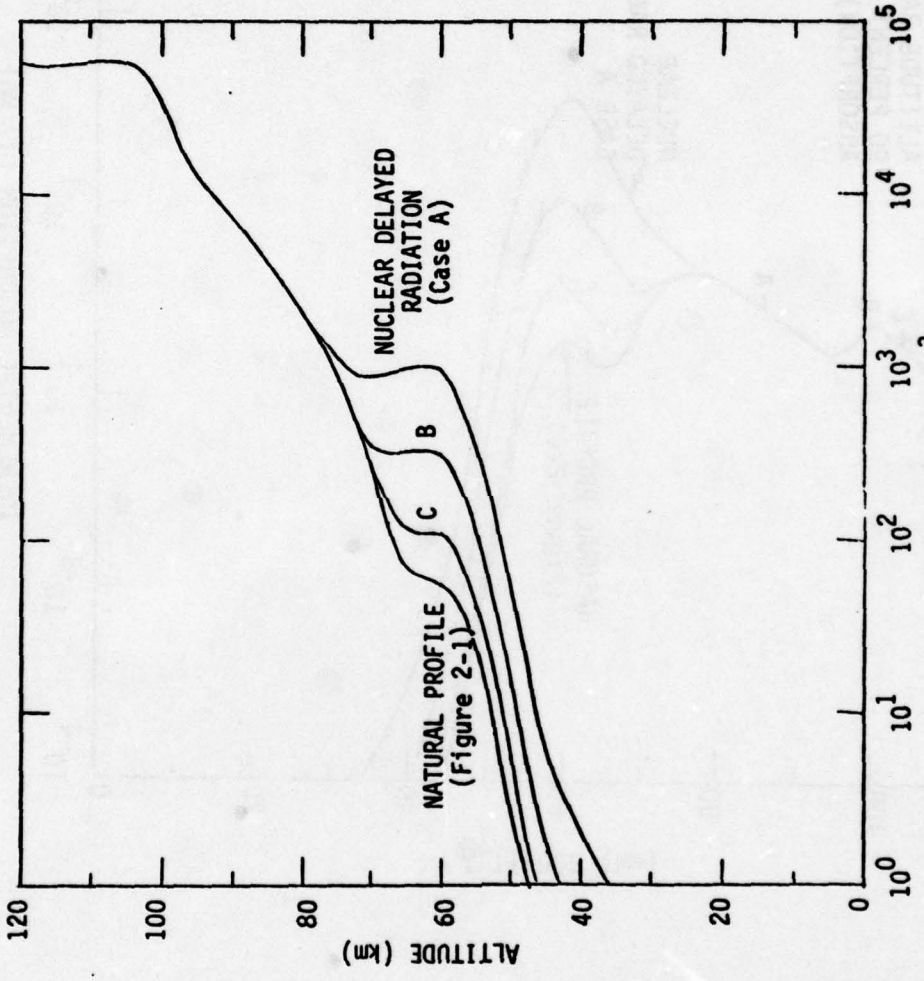

Figure 2-12. Enhanced electron concentration profiles due to radioactive nuclear fission sources.

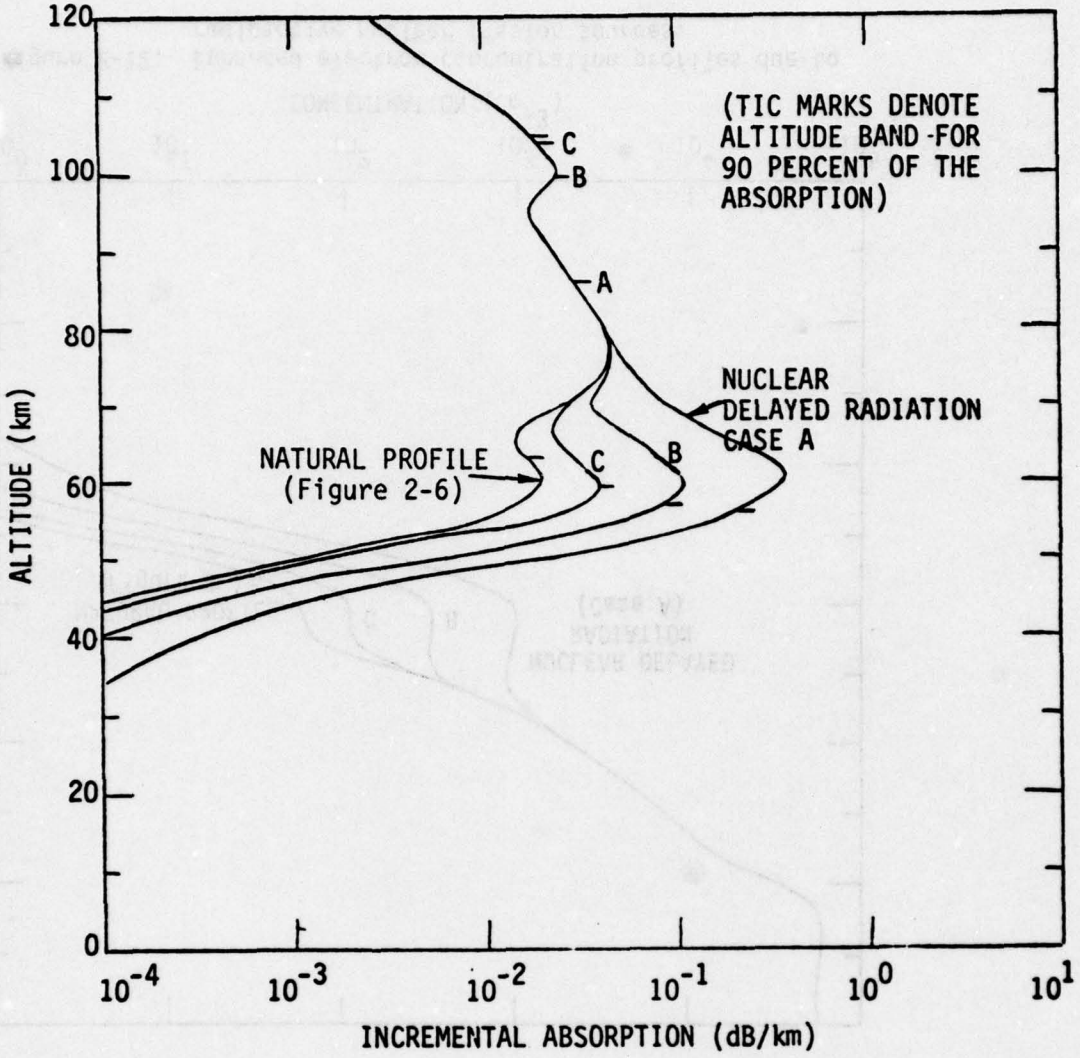

Figure 2-13. Enhanced wave absorption at 10 MHz due to radioactive nuclear fission sources.

output shows that in the nuclear cases D changes at most about 1 percent from that shown in Figure 2-8, due to slight changes in the relative proportions of negative ions from those shown in Figure 2-9. (The absolute magnitude of each ion concentration increases in the nuclear cases, of course.) The value of the electron-ion recombination rate α_d changes a little more. In the larger (Case A) nuclear case, α_d is reduced about 10 percent from that shown in Figure 2-8 in the altitude regime between 50 and 70 km. This is due to slightly higher proportions of ions such as $NO^+(N_2)$ and $NO^+(W)_2$ which have lower recombination rates than the dominant ions $H_3O^+(W)_2$ and $H_3O^+(W)_3$. The attachment rate A and the ion-ion recombination rate α_i are independent of q and remain as shown in Figure 2-8.

The simplified interpretation of the lumped parameter solution for the undisturbed case (see Equations 2-5 and 2-6 above) can be seen to remain valid for the nuclear disturbed cases also. Even with the larger values for q, we still have $D >> \sqrt{q\alpha}$ throughout the absorbing region. Thus, the crossover between D and A determines the lower boundary of the absorbing region, and throughout most of the absorbing region we have $(e) = \sqrt{q/\alpha_d}$. Thus, in the sensitivity analyses, we shall address the effect of the minor neutral species on the parameters A, D, q, and α_d.

SECTION 3
SENSITIVITY ANALYSIS

This section presents an investigation into the sensitivity of the HF wave absorption to variations in the atmospheric minor neutral species, and an analysis of the observed sensitivity in terms of the ionospheric chemistry model parameters. In anticipation of this investigation, atmospheric data on the expected variations in minor neutral species has been collected and collated (Reference 3-1). Unfortunately, most of the available data is for the stratosphere (below about 50 km altitude) or the lower thermosphere (above about 80 km altitude). In the important mesosphere region (50 to 80 km altitude) where much of the HF wave absorption takes place—particularly in the nuclear disturbed cases—there is very little empirical data. Theoretical models for the minor neutral species concentrations are not reliable for absolute predictions because they are highly sensitive to transport processes (molecular or turbulent diffusion, gross wind patterns) that are difficult to model. Thus we have chosen somewhat crude bounds for the minor neutral species concentration variations to be employed in the sensitivity analysis, based on a combination of extrapolated empirical data and reasoning from the theoretical models.

Since ionospheric absorption of HF waves is significant only in the daytime, we shall concentrate on the daytime conditions. Figure 3-1 shows mean daytime profiles (Reference 3-2) of the minor atmospheric species considered in the analysis.

Reference 3-1. Jordano, R.J., and H.H. Rutherford, *Suggested Natural Variations in Atmospheric Minor Neutral Species*, GE78TMP-26 (ARBRL-CR-00375), General Electric Company—TEMPO, July 1978.

Reference 3-2. Myers, B.F., *The ROSCOE Manual, Volume 14b-Midlatitude Density Profiles of Selected Atmospheric Species*, SAI-75-609-LJ-2B (DNA 3964F-14b), Science Applications, Inc., June 1975.

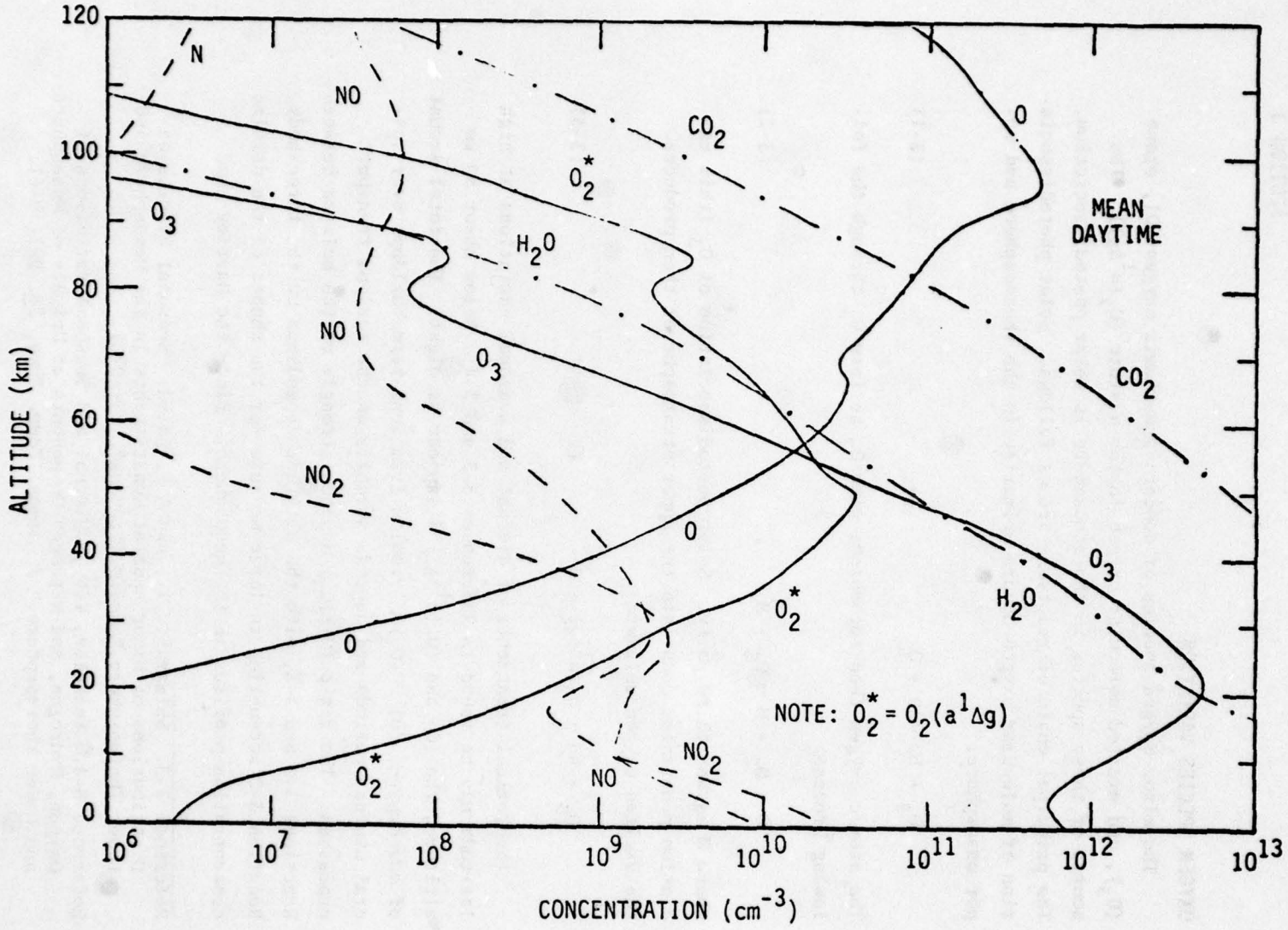

Figure 3-1. Mean daytime atmospheric minor neutral species profiles.

OXYGEN SPECIES VARIATION

The minor oxygen species of concern are atomic oxygen (O), ozone (O_3), and excited molecular oxygen in the a-state ($O_2(a^1\Delta g)$). The source of these species in the atmosphere is solar photodissociation. The principal chain of reactions are as follows. Solar photodissociation of molecular oxygen occurs primarily in the thermosphere and upper mesosphere:

$$O_2 + h\nu \rightarrow O + O \qquad (3\text{-}1)$$

The atomic oxygen then recombines with O_2 to form O_3 through the following process:

$$O + O_2 + M \rightarrow O_3 + M \qquad (3\text{-}2)$$

where M is any third party. Solar photodissociation of O_3 (this radiation penetrates down into the upper stratosphere) then produces the excited oxygen molecule:

$$O_3 + h\nu \rightarrow O_2(a^1\Delta g) + O \qquad (3\text{-}3)$$

Theoretical treatments of diurnal and seasonal variations at high latitude may be found in References 3-3 and 3-4. Below about 80 km altitude, the (O) and ($O_2(a^1\Delta g)$) disappear at night. The total amount of *odd oxygen*, (O) + (O_3), results from long-term buildups over several diurnal periods and depends strongly on the various transport processes. The ratio (O)/(O_3) depends strongly on the balance between Reactions 3-2 and 3-3, with the altitude dependence on the three-body Reaction 3-2 accounting in large measure for the shapes of the daytime concentration profiles in the mesosphere. Since the Hartley band

---

Reference 3-3. Shimazaki, T., and A.R. Laird, "Seasonal Effects on Distributions of Minor Neutral Constituents in the Mesosphere and Lower Thermosphere," *Radio Science* 7, 23(1972).

Reference 3-4. Koshelev, V.V., "Diurnal and Seasonal Variations of Oxygen, Hydrogen, and Nitrogen Components at Heights of Mesosphere and Lower Thermosphere," *J. Atmos. Terr. Phys.* 38, 991(1976).

radiation that dissociates the O_3 penetrates below 60 km, we expect little dependence on solar zenith angle in the absorbing region except very near sunrise or sunset. Thus the ratio $(O)/(O_3)$ and $(O_2(a^1 g))/(O_3)$ are relatively constant throughout the day and there should be a positive correlation between the variations in these species (as seen on the longer time scale or over spatial coordinates).

Based on the empirical data, we have chosen a simple variation of plus or minus a factor of 3 (over the whole profile) to be representative of the expected latitude, season, or solar cycle variations in the daytime concentrations of the minor oxygen species. The general trend is for the concentrations to be reduced at higher latitudes. There is some confusion as to the seasonal variations, both in theory (see References 3-3 and 3-4) and in the measurements (see Reference 3-1).

Table 3-1 presents the sensitivity of the integrated one-way vertical HF absorption to variations in the oxygen species. Several cases

Table 3-1. Integrated one-way vertical 10 MHz absorption with variation of oxygen species.

Species Variation	Natural (dB)	Nuclear (dB)
Base Case	1.41	5.10
3X Increase (O_3), (O_2^*)	1.43	5.32
3X Increase (O)	1.60	6.92
3X Increase (O), (O_3), (O_2^*)	1.61	7.04
1/3 X Decrease (O_3), (O_2^*)	1.40	4.91
1/3 X Decrease (O)	1.31	3.86
1/3 X Decrease (O), (O_3), (O_2^*)	1.29	3.62

Note:
$(O_2^*) = (O_2(a^1\Delta g))$

are listed which are variations from the natural ionosphere case shown in Figure 2-6, and from the largest nuclear case (Case A) of Figure 2-13. In each case, we investigate a variation of the (O) profile, the (O_3) and $(O_2(a^1\Delta g))$ profiles, and then all three profiles at once. Note that the sensitivity due to the (O) variation is stronger than that due to (O_3) and $(O_2(a^1\Delta g))$, and that the sensitivity is larger in the nuclear case than under natural conditions. We shall analyze this behavior in terms of the model parameters.

Figure 3-2 shows vertical profiles of the incremental absorption for the natural and nuclear cases of maximum variation in Table 3-1. Note that most of the sensitivity occurs at altitudes below 65-70 km, with the peak variation in incremental absorption maximizing at about a factor of 10 at 50 km altitude. This altitude regime contributes a small portion of the total integrated absorption in the natural case, but contributes a major portion of the integrated absorption in the nuclear case. This explains the larger sensitivity of the nuclear case noted in Table 3-1.

In analyzing the results further, we shall employ the effective lumped parameter concepts discussed in Section 2. Recall that the incremental absorption is proportional to the electron concentration (e), and that

$$(e) = \frac{D}{D+A}\sqrt{q/\alpha_d} \qquad (3\text{-}4)$$

through most of our regime of interest.

In the altitude regime below 65-70 km, the oxygen species variations act through the effective detachment rate D. The effects of changes in D are washed out at higher altitudes because for small A the ratio D/(D+A) goes to unity in all cases. Changes in D can result from changes in the detachment rates for particular negative ions, or from changes in the relative proportions of ions with different detachment rates (see Equation A-34). Figure 3-3 shows the contribution of each negative ion rate to the total effective D for the base case condition. (Figure 3-3 is for the natural ionosphere case, but is very

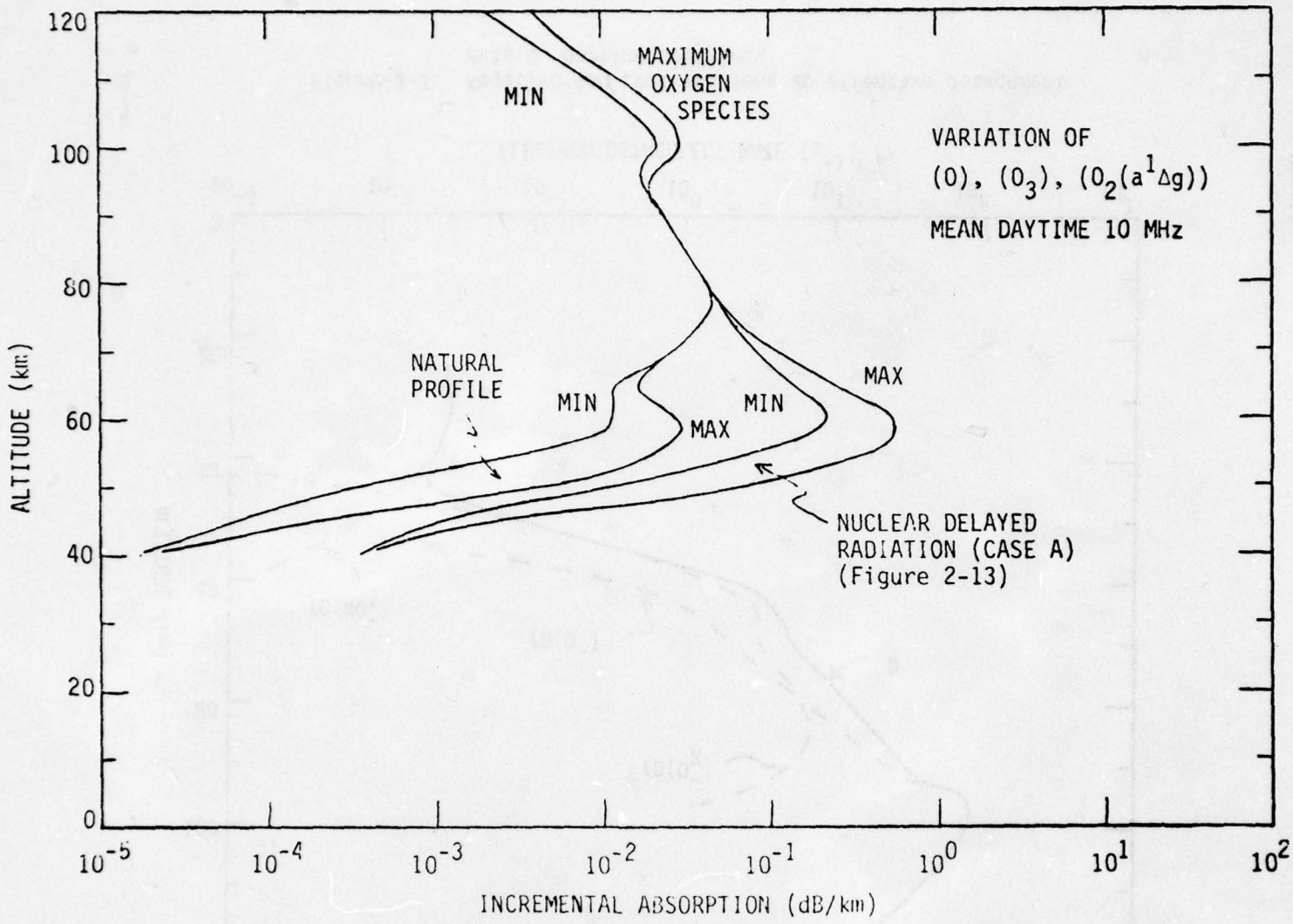

Figure 3-2. Wave absorption profiles with variation of oxygen species.

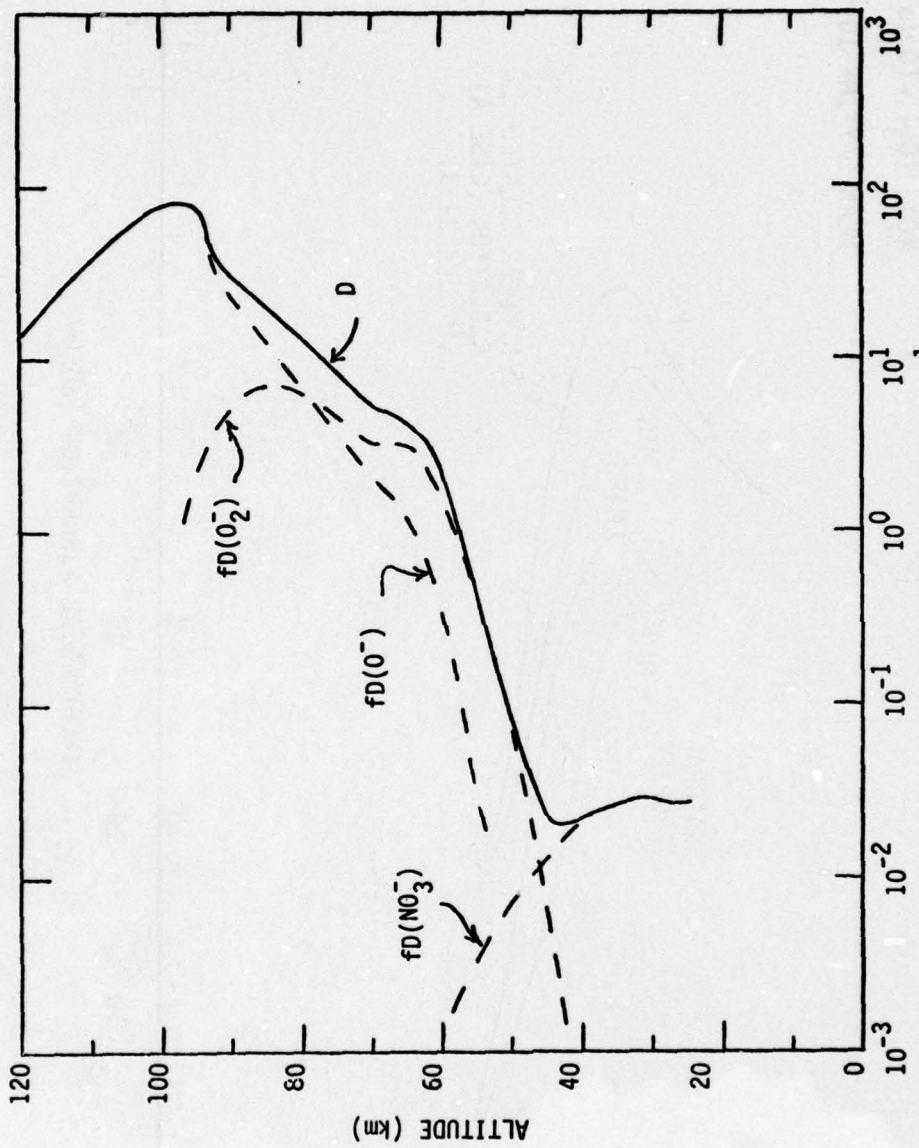

Figure 3-3. Negative ion contributions to effective detachment rate D, daytime profiles.

representative of the nuclear cases also since the relative distribution of negative ions is a weak function of q.) Note that the important ions are O_2^- and O^- at altitudes where the HF absorption occurs. Other ions have larger concentrations, but have negligible detachment rates (Equations A-12 to A-21).

Figure 3-4 shows the contributions of specific chemical reactions to the detachment rates for O_2^- and for O^-. Note the strong dependence on (O) and $(O_2(a^1\Delta g))$. Because most of the sensitivity shown in Figure 3-2 occurs below 60 km, we would expect the $(O_2(a^1\Delta g))$ variations to have more impact than the (O) variations, contrary to the results of Table 3-1. The answer lies in the different ways these species affect the relative distribution of negative ions. The increase of (O_3) and $(O_2(a^1\Delta g))$ tend to decrease the relative concentrations of O_2^- and O^-, compensating for the increase in the detachment rates of those species. The increase of (O) tends to increase the relative concentrations of O_2^- and O^-, however, enhancing the effectiveness of their detachment rates in contributing to D. For example, increasing (O_3) and $(O_2(a^1\ g)$ by a factor of 3 increases the O_2^- and O^- detachment rates about a factor of 2 to 3 between 50 and 60 km altitude (Figure 3-4). This also decreases the relative concentrations of O_2^- and O^- about a factor of 2, however (base case distributions are shown in Figure 2-9), leaving a net increase of D of, at most, 50 percent. Increasing (O) by a factor of 3 increases the O_2^- and O^- detachment rates less than a factor of 2 between 50 and 60 km altitude. This also increases the relative concentrations of O_2^- and O^- in this regime by a factor of 1.5 to 3, giving typical increases in D more than a factor of 3.

It is difficult to identify the key chemical reactions responsible for these shifts in relative concentrations of O_2^- and O^-, because all the ions are coupled by a network of transfer reactions (see Figure A-2). A survey of the transfer rates involving the minor neutral species shows the following candidates for the production of O_2^- and O^-:

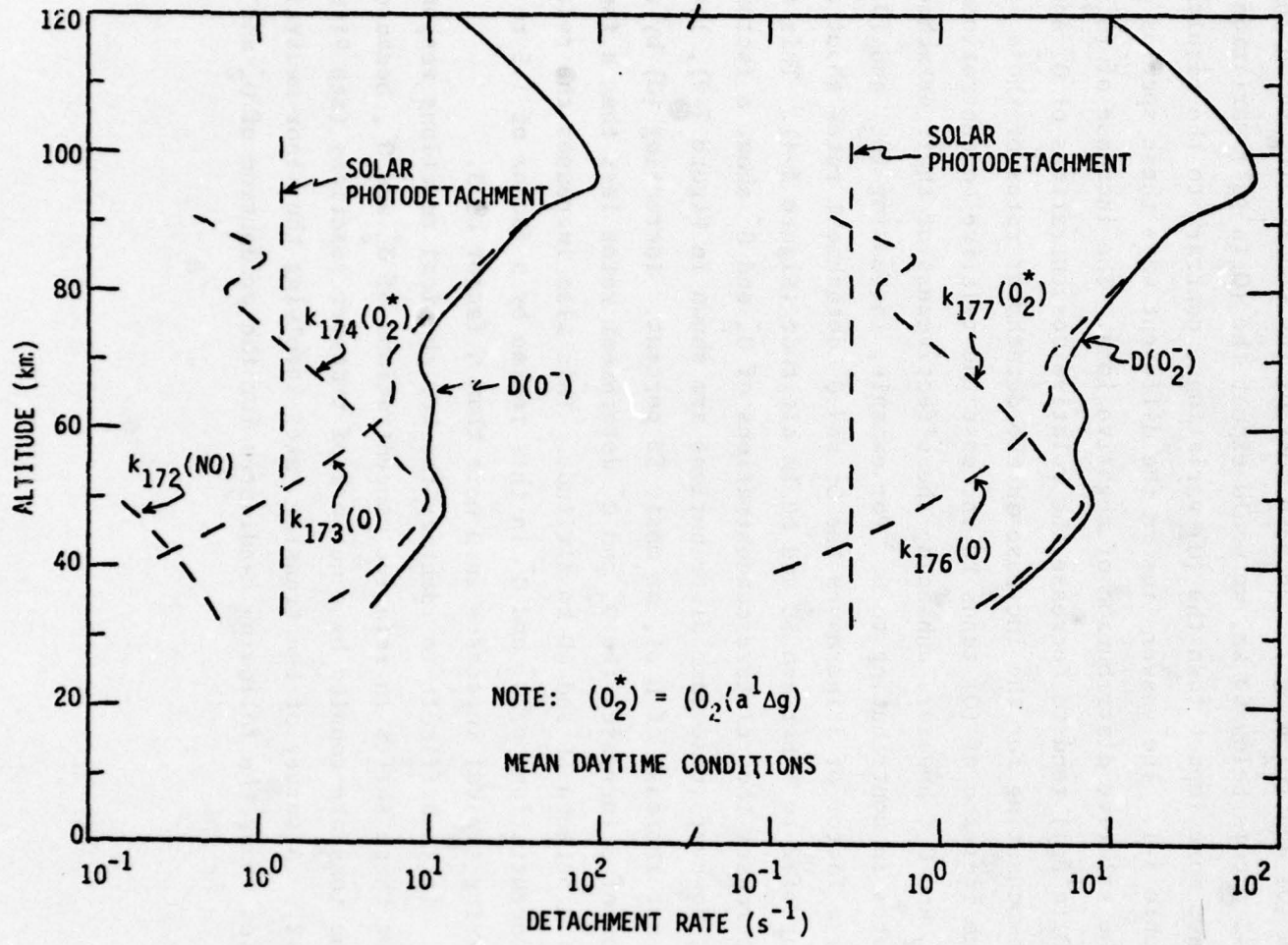

Figure 3-4. Daytime detachment rate profiles for (O^-) and (O_2^-).

$$O_3^- + O \rightarrow O_2^- + O_2 \qquad (k_{234} = 2.5 \times 10^{-10}) \qquad (3\text{-}5)$$

$$CO_3^- + O \rightarrow O_2^- + CO_2 \qquad (k_{203} = 1.1 \times 10^{-10}) \qquad (3\text{-}6)$$

$$O_2^- + O \rightarrow O^- + O_2 \qquad (k_{223} = 1.5 \times 10^{-10}) \qquad (3\text{-}7)$$

Since CO_2^- is a dominant ion in this regime, the second reaction (k_{203}) is most likely the key one. The third reaction (k_{223}) would share the increase with (O^-). Two candidate reactions contribute to the loss of O_2^- and O^-:

$$O_2^- + O_3 \rightarrow O_3^- + O_2 \qquad (k_{226} = 4.0 \times 10^{-10}) \qquad (3\text{-}8)$$

$$O^- + O_3 \rightarrow O_3^- + O \qquad (k_{218} = 5.3 \times 10^{-10}) \qquad (3\text{-}9)$$

The first reaction (k_{226}) contributes 30 to 40 percent of the (O_2^-) loss rate in this regime. The second (k_{218}) contributes 15 to 20 percent of the loss rate of (O^-).

We make one final note with regard to the small variations in incremental absorption at the higher altitudes, above 90 km, in Figure 3-2. These are due to two factors related to the atomic oxygen concentration. One is the direct ionization of (O) by solar UV (Equation B-24). This represents about 5 percent of the total UV ionization source at above 100 km, for example (see Figure 2-1). The second factor is the influence of (O) on the charge transfer from (N_2^+) to (O_2^+) or (NO^+) (Equations A-1 and A-2, specifically terms P_5 and P_6). This has negligible effect on the ratio (NO^+)/(O^+), however, because the primary source of (NO^+) is from charge transfer from O_2^+ in either case. (A change in the ratio (NO^+)/(O_2^+) would have affected α_d).

ODD NITROGEN SPECIES VARIATION

The minor nitrogen species of concern are atomic oxygen (N), nitric oxide (NO), and nitrogen dioxide (NO_2). Figure 3-1 shows mean daytime profiles for these species concentrations (Reference 3-2). Potential

sources of these species in the upper atmosphere are ion-transfer and ion-recombination reactions, and solar photodissociation of N_2, although the quantitative aspeces of the various production mechanisms are not well understood (Reference 3-5). The ion sources would be in the thermosphere (above 100 km altitude) and would include the following reactions:

$$N_2^+ + e \rightarrow N(^2D) + N(^4S) \qquad (3\text{-}10)$$

$$N_2^+ + O \rightarrow NO^+ + N(^4S \text{ or } ^2D) \qquad (3\text{-}11)$$

$$O^+ + N_2 \rightarrow NO^+ + N(^4S \text{ or } ^2D) \qquad (3\text{-}12)$$

$$NO^+ + e \rightarrow O + N(^4S \text{ or } ^2D) \quad . \qquad (3\text{-}13)$$

The excited atomic nitrogen then reacts rapidly with molecular oxygen to form nitric oxide:

$$N(^2D) + O_2 \rightarrow NO + O \quad . \qquad (3\text{-}14)$$

The principal sinks for odd nitrogen at these altitudes are transport processes (downward flux of (NO) into the mesosphere exceeds 10^8 cm^2 s^{-1}) and the following chemical reaction

$$(N^4S) + NO \rightarrow N_2 + O \quad . \qquad (3\text{-}15)$$

From the last two reactions, we see that the relative abundance of ionospheric (N) versus (NO) depends critically on the assumed branching ratios (to $N(^4S)$ or $N(^2D)$) in the ion reactions. Most theoretical models favor the $(N(^2D))$, and thus give very low ionospheric concentrations of (N) compared to (NO) below 120 km altitude. Empirical

Reference 3-5. Strobel, D.F., "Minor Neutral Constituents in the Mesosphere and Lower Thermosphere," *Radio Science* 7, 1 (1972).

measurements of (N) have not substantiated this condition. In fact, they give (N) concentrations typically 3 orders of magnitude higher than the calculations (Reference 3-1). The measurements are difficult however, because the *in situ* techniques are subject to contamination.

In the mesosphere, the important reactions (assuming (N) is negligible) are:

$$NO + O_3 \rightarrow NO_2 + O_2 \qquad (3\text{-}16)$$

$$NO_2 + O \rightarrow NO + O_2 \qquad (3\text{-}17)$$

$$NO_2 + h\nu \rightarrow NO + O \qquad (3\text{-}18)$$

$$NO + O \rightarrow NO_2 + h\nu \qquad (3\text{-}19)$$

$$NO + O + M \rightarrow NO_2 + M \quad . \qquad (3\text{-}20)$$

Note that all the reactions just convert between (NO) and (NO_2) so that (on a time scale shorter than the diurnal) the total (NO) + (NO_2) is constant. The ratio $(NO)/(NO_2)$ is controlled by solar photodissociation of (NO_2) and by the ratio $(O)/(O_3)$. Below 70 km, the NO is converted to NO_2 at night. Theoretical calculations (Reference 3-3) show that above about 50 km altitude, the (NO) is fairly constant throughout the day, with the diurnal transition occurring abruptly at sunrise and sunset. The (NO_2) shows a stronger dependence on solar zenith angle during the day due to the photodissociation process. Thus, time of day must be considered when comparing latitudinal, seasonal, or solar cycle variations in (NO_2). For a given solar zenith, however, we expect positive correlation between the variations in (NO) and (NO_2).

Empirical data (Reference 3-1) indicate that variation in (NO) and (NO_2) are probably larger than those in (O) and (O_3). There is a definite increase in (NO) and (NO_2) at high latitudes, which appears to

be related to auroral activity (Reference 3-6). Seasonal data tend to favor maximum concentrations in summer. To simplify comparison to the oxygen species sensitivity, we have varied the (NO) and (NO_2) by the same factor of 3 in this portion of the analysis. We shall discuss the potential effect of the very large uncertainty in (N) toward the end of this section.

Table 3-2 presents the sensitivity of the integrated one-way vertical HF absorption to variations in the (NO) and (NO_2). The cases

Table 3-2. Integrated one-way vertical 10 MHz absorption with variation of nitrogen species.

Species Variation	Natural (dB)	Nuclear (dB)
Base Case	1.41	5.10
3 X increase (NO), (NO_2)	2.05	5.52
1/3 X decrease (NO), (NO_2)	1.10	4.91

listed are variations of the natural ionosphere case shown in Figure 2-6, and from the largest nuclear case (Case A) of Figure 2-13. In contrast to the observed sensitivity to oxygen species (Table 3-1), the effect of the nitrogen species variation is stronger for the natural ionosphere than for the nuclear-disturbed ionosphere.

Figure 3-5 shows vertical profiles of the incremental absorption for each of the cases of Table 3-2. Note that the largest sensitivity is in the altitude band between 65 and 95 km and there is a crossover in the correlation above 100 km altitude. In terms of the lumped parameters (Equation 3-4), the impact of the nitrogen species is principally through the ion production rate q. There is some smaller effect through the electron recombination rate α_d, and an almost negligible effect through the detachment rate D.

Reference 3-6. Gerard, J.C., and C.A. Barth, "High-Latitude Nitric Oxide in the Lower Thermosphere," *J. Geophys. Res.* 82, 674 (1977).

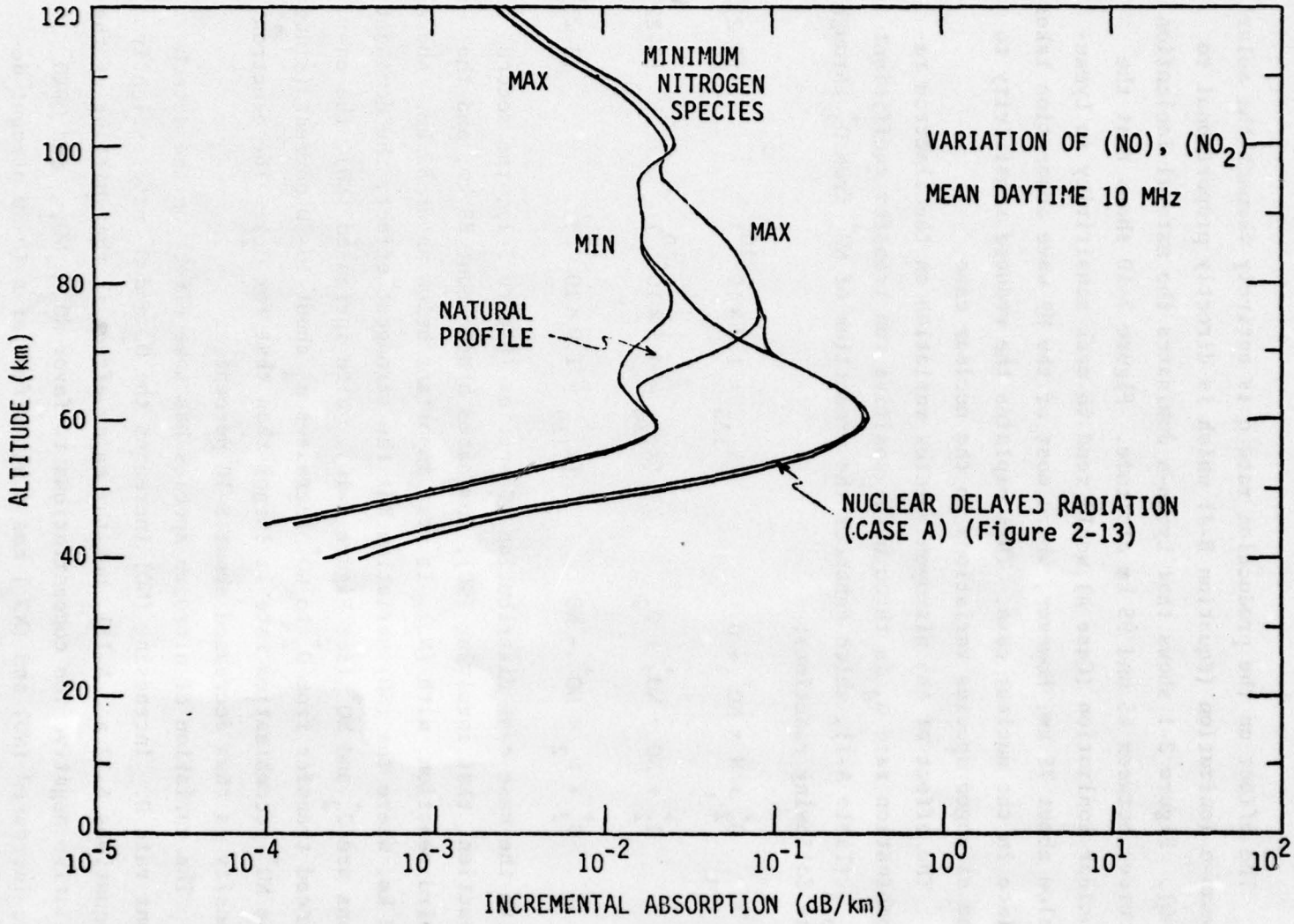

Figure 3-5. Wave absorption profiles with variation of nitrogen species.

The effect on the production rate q is entirely through the solar Lyman-α ionization (Equation B-4) which is directly proportional to (NO). Figure 2-1 shows that Lyman-α dominates the natural ionization sources between 65 and 95 km altitude. Figure 2-10 shows that the nuclear ionization (Case A) would tend to mask sensitivity to Lyman- below about 75 km, however, where most of the HF wave absorption takes place in the nuclear case. This explains the reduced sensitivity to the nitrogen species variations in the nuclear case.

The effect of the nitrogen species variation on the electron recombination rate α_d is through the positive ion transfer coefficient T_{p14} (Table A-1), which enhances the production of NO^+ from O_2^+ through the following reactions:

$$O_2^+ + N \rightarrow NO^+ + O \qquad (k_{135} = 1.2 \times 10^{-10}) \qquad (3\text{-}21)$$

$$O_2^+ + NO \rightarrow NO^+ + O_2 \qquad (k_{136} = 4.5 \times 10^{-10}) \qquad (3\text{-}22)$$

$$O_2^+ + N_2 \rightarrow NO^+ + NO \qquad (k_{139} = 1.0 \times 10^{-16}) \qquad (3\text{-}23)$$

With the base case distribution of species (Figure 3-1), the second reaction, that involving (NO), dominates above about 85 km, and the third reaction, with (N_2), is most important below about 85 km. Above 90 km, where the (NO) variation has the strongest effect, the dominant ions are O_2^+ and NO^+ (see Figure 2-10). With increased (NO), the enhanced transfer from O_2^+ to NO^+ increases α_d about 10-20 percent (since the NO^+ recombination rate is larger than that for O_2^+). The electron density is thus decreased about 5-10 percent.

The variation of nitrogen species has some effect on the detachment rate D. Increasing (NO) increases the O_2^- and O^- rates slightly (Equations A-12 and A-13), but the major effect is the shifting of the relative negative ion concentrations to favor NO_2^-, NO_3^-, and $OONO^-$. The increased (NO) and (NO_2) has a net effect of a 10-20 percent decrease in D in the altitude band between 50 and 65 km where the value of D is important.

We now address the sensitivity to the atomic nitrogen (N). We have not displayed the results, but the effect of (N) on the HF absorption is entirely through the positive ion transfer of Equation 3-21. The rate coefficient is about one-fourth that for the transfer involving (NO) (Equation 3-22) and one can see from Figure 3-1 that increasing (N) about two orders of magnitude would make it competitive with (NO). The net effect of the very large (N) would then be to shift the relative ion concentrations from O_2^+ to NO^+ above about 95 km altitude, increasing α_d and decreasing the electron concentration and HF wave absorption in this region. The maximum possible reduction in absorption due to this effect would be about 10-15 percent reduction of that portion above 95 km. This is an insignificant effect even in the natural ionosphere case.

WATER VAPOR AND CARBON DIOXIDE VARIATIONS

There are insufficient data upon which to base estimates of expected variations in thes species (Reference 3-1). In the mesosphere and lower thermosphere, where most HF wave absorption occurs, there are almost no empirical measurements and estimates of the concentrations are based on model calculations. Consequently, we have chosen to use a simple factor of 3 variation of the profiles of Figure 3-1 to facilitate comparison of sensitivities to the other species.

Table 3-3 presents the sensitivity of the integrated one-way vertical HF absorption to variations in the (H_2O) and (CO_2) profiles. The cases listed are variations of the natural ionosphere case shown in Figure 2-6, and from the largest nuclear case (Case A) of Figure 2-13. Note that increases in either the (H_2O) or (CO_2) cause a decrease in the HF absorption. Both the (H_2O) and (CO_2) variations cause about 5 percent variation in absorption in the natural ionosphere case. In the nuclear case, the effect of the (CO_2) variation is reduced slightly, and the effect of the (H_2O) variation is enhanced slightly.

Figure 3-6 shows vertical profiles of the incremental absorption for each of these cases. Note that the sensitivity to (CO_2) is almost entirely in the short altitude band between 75 and 90 km, while the

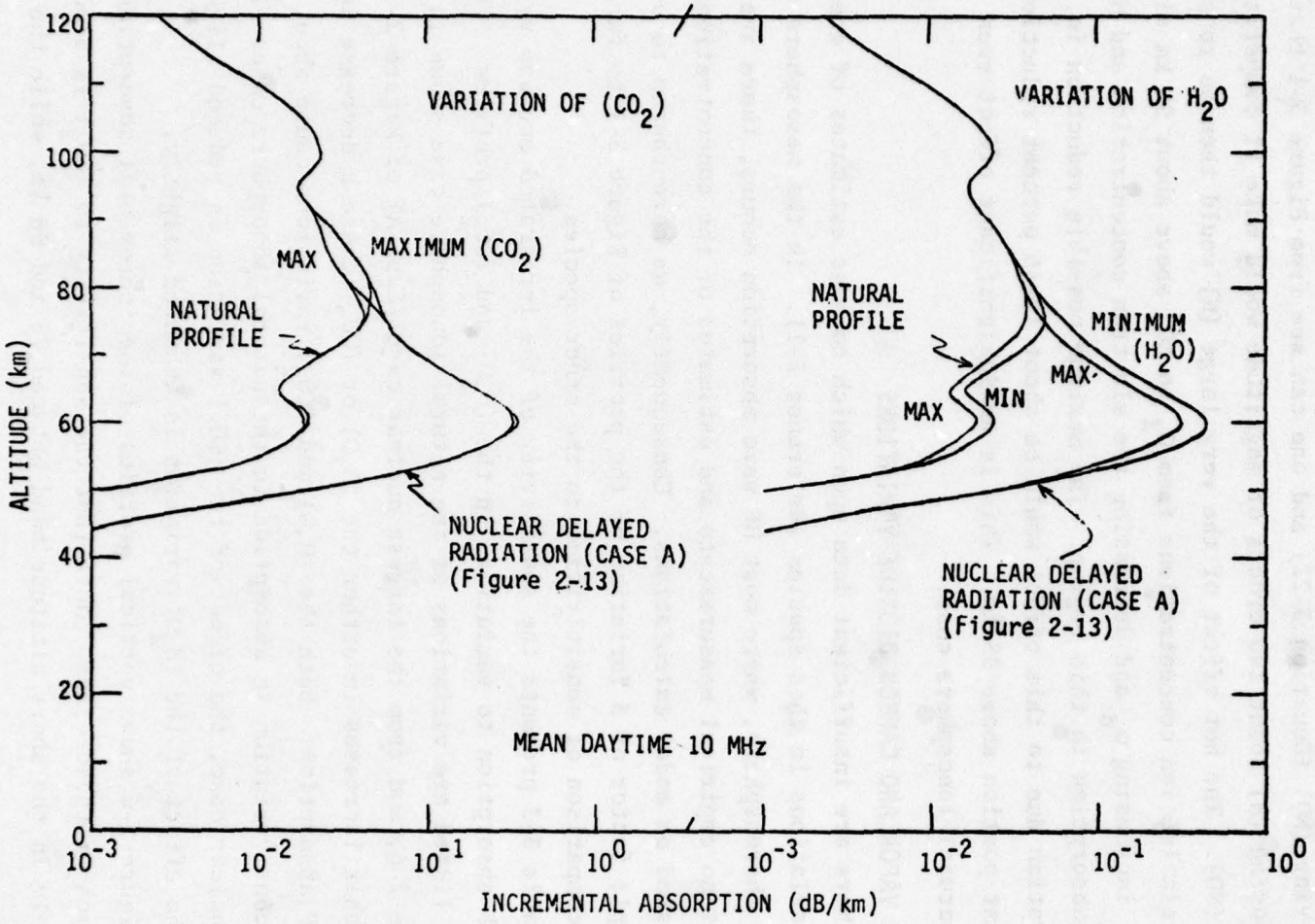

Figure 3-6. Wave absorption profiles with variation of (H_2O) and (CO_2).

Table 3-3. Integrated one-way vertical 10 MHz absorption with variation of (H_2O) and (CO_2).

Species Variation	Natural (dB)	Nuclear (dB)
Base Case	1.41	5.10
3 X increase (H_2O)	1.36	4.79
1/3 X decrease (H_2O)	1.49	5.82
3 X increase (CO_2)	1.36	4.88
1/3 X decrease (CO_2)	1.48	5.25

sensitivity to (H_2O) variation is at altitudes between 55 and 80 km. The absorption in the nuclear case is thus more sensitive to (H_2O) because the nuclear enhancement is entirely within the lower region.

The impact of the (CO_2) variation is through α_d (see Equation 3-4). The important reaction is

$$NO^+ + CO_2 + M \rightarrow NO^+(CO_2) + M \qquad (3\text{-}24)$$

Larger (CO_2) enhances the transfer from (NO^+) to ($NO^+(CO_2)$) which has a larger electron recombination rate (by a factor of 4, compare k_{157} and k_{160} in Appendix A). The ($NO^+(CO_2)$) is lumped with the ($NO^+(N_2)$)-group in Figure 2-10. They are lumped together for convenience in the model because they have similar recombination rates (see Equation A-30). From Figure 2-10 then, we see that the important interplay between the relative concentration of $NO^+(CO_2)$ and other ions is in the altitude regime 75-90 km.

The (CO_2) also has influence on the shift in negative ion concentration to favor (CO_3^-) and (CO_4^-) instead of (O^-) and (O_2^-). See T_{n19} and T_{n33} in Table A-2. This decreases the effective detachment D, but the magnitude of the change is negligible in the model.

The impact of the (H_2O) variation is also through α_d. Dozens of positive ion transfer coefficients involving (H_2O) favor the transition to higher order hydrates of the ions NO^+ and H_3O^+. (See Table A-1). Higher order hydrated ions tend to have larger electron recombination rates, as shown in Section 2 (see list preceeding Equation 2-5). The largest rates are more than an order of magnitude larger than those for the simple ions O_2^+ and NO^+. From Figure 2-10, we see that the various hydrated ions begin to become important below about 80-km altitude, consistent with the onset of the (H_2O) sensitivity in Figure 3-6.

APPENDIX A
THE CHEMISTRY MODEL

The chemistry model employed for calculations in this report is the steady-state ion chemistry model taken from the ROSCOE/WEPH computer programs (References A-1 and A-2). We summarize the properties of the model here for the reader's convenience. Note in particular that neutral species are inputs for this part of the model, and are assumed to be unaffected by the ion solutions.

The positive and negative ions treated explicitly in the model are illustrated in Figures A-1 and A-2, along with a schematic representation of the positive ion and negative ion transfer reactions. The numbers next to the arrowheads indicate the ion transfer coefficients which are defined in Tables A-1 and A-2. Additional reactions not shown in Figures A-1 and A-2 include positive ion production due to natural or nuclear energy deposition, the production of negative ions by electron attachment to neutral species, the loss of negative ions due to electron detachment, and recombination of positive ions and electrons. All reactions and rate coefficients are given in Table A-3.

The ion production models due to natural or nuclear energy deposition provide "primary" ion production rates $q(N^+)$, $q(O^+)$, $q(N_2^+)$, $q(O_2^+)$, and $q(NO^+)$. The first three species (N^+, O^+, and N_2^+) are assumed to

Reference A-1. Knapp, W.S., et al, *WEPH VI: A Fortran Code for the Calculation of Ionization and Electromagnetic Propagation Effects Due to Nuclear Detonations (U), Volume 3—Computational Models (U)*, GE75TMP-53 (DNA 3766T-3), General Electric Company—TEMPO, October 1976 (Confidential/Formerly Restricted Data).

Reference A-2. Knapp, W.S., et al, *The ROSCOE Manual: Volume II—Atmospheric Chemistry Models*, GE74TMP-59 (DNA 3964F-11), General Electric Company—TEMPO (to be published).

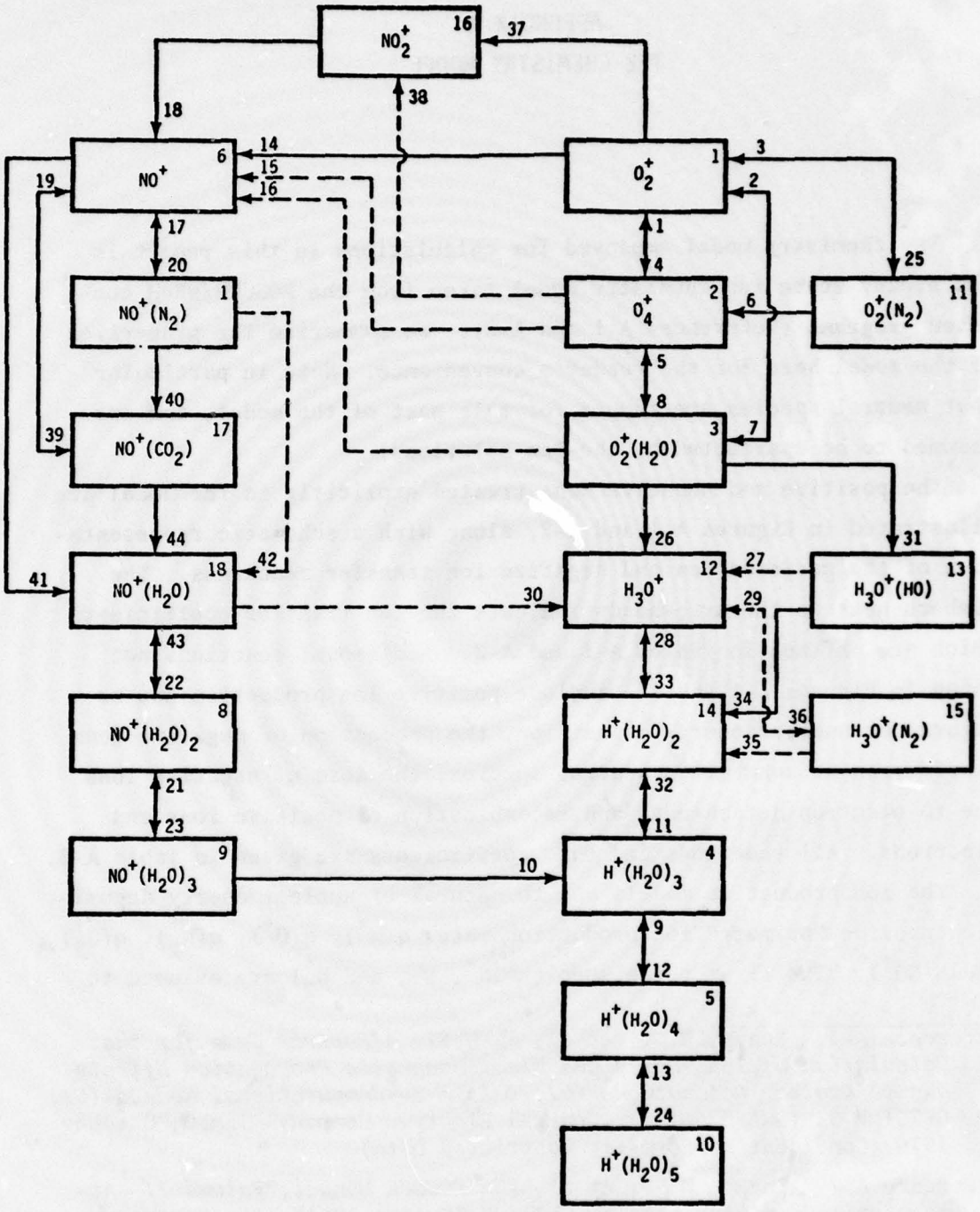

NOTE: NUMBERS REFER TO THE POSITIVE ION SPECIES AND POSITIVE ION TRANSFER COEFFICIENTS

Figure A-1. Positive ion transfer coefficients.

Figure A-1. Continued (notes).

Ion Number*	Ion Number*																
	1	2	3	4	5	6	7	8	9	10	11	12	13	14	15	16	17	18
1		1	2								3							
2	4		5								6							
3	7	8																
4					9				10					11				
5				12						13								
6	14	15	16				17									18	19	
7						20												
8									21									22
9								23										
10					24													
11	25																	
12		26											27	28	29			30
13		31																
14			32									33	34			35		
15												36						
16	37	38																
17						39	40											
18						41	42	43										

*1	O_2^+	7	$NO^+(N_2)$	13	$H_3O^+(HO)$	
2	O_4^+	8	$NO^+(H_2O)_2$	14	$H^+(H_2O)_2$	
3	$O_2^+(H_2O)_3$	9	$NO^+(H_2O)_3$	15	$H_3O^+(N_2)$	
4	$H^+(H_2O)_3$	10	$H^+(H_2O)_5$	16	NO_2^+	
5	$H^+(H_2O)_4$	11	$O_2^+(N_2)$	17	$NO^+(CO_2)$	
6	NO^+	12	H_3O^+	18	$NO^+(H_2O)$	

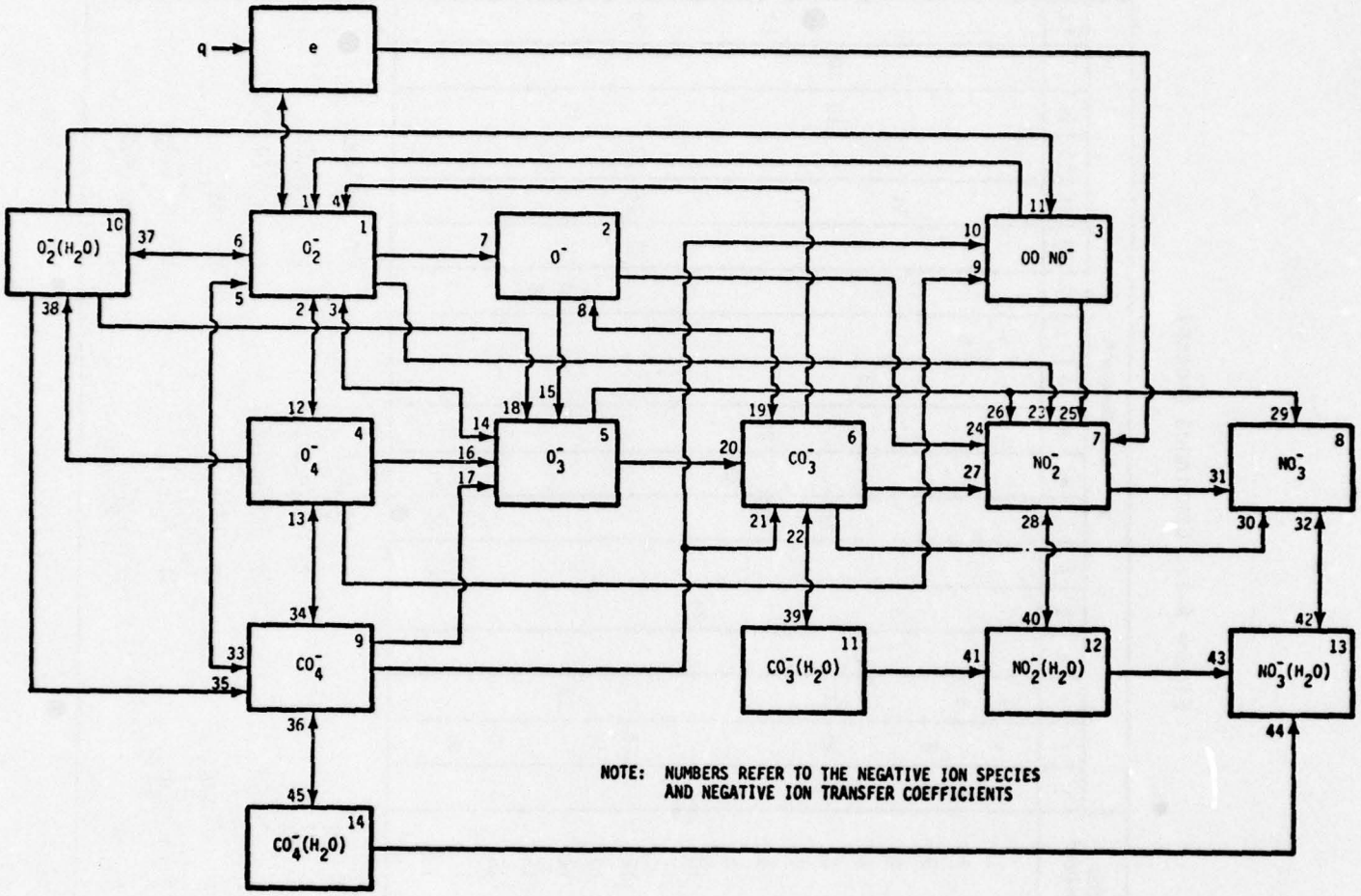

Figure A-2. Negative ion transfer coefficients.

Figure A-2. Continued (notes).

Ion Number*	Ion Number*													
	1	2	3	4	5	6	7	8	9	10	11	12	13	14
1			1	2	3	4			5	6				
2	7					8								
3				9					10	11				
4	12								13					
5	14	15		16					17	18				
6		19			20				21		22			
7	23	24	25		26	27						28		
8					29	30	31						32	
9	33			34						35				36
10	37			38										
11						39								
12							40				41			
13								42				43		44
14									45					

*1	O_2^-	6	CO_3^-	11	$CO_3^-(H_2O)$
2	O^-	7	NO_2^-	12	$NO_2^-(H_2O)$
3	$OONO^-$	8	NO_3^-	13	$NO_3^-(H_2O)$
4	O_4^-	9	CO_4^-	14	$CO_4^-(H_2O)$
5	O_3^-	10	$O_2^-(H_2O)$		

Table A-1. Positive ion transfer coefficients.

$T_{p1} = k_{143}(M) + k_{153}(O)$

$T_{p2} = k_{147}(O_2(^1\Delta))$

$T_{p3} = k_{141}(M)$

$T_{p4} = k_{142}(O_2)(M)$

$T_{p5} = k_{150}(O_2)$

$T_{p6} = k_{148}(O_2)$

$T_{p7} = k_{134}(H_2O)(M)$

$T_{p8} = k_{149}(H_2O)$

$T_{p9} = k_{109}(M)$

$T_{p10} = k_{126}(H_2O)$

$T_{p11} = k_{106}(H_2O)(M)$

$T_{p12} = k_{108}(H_2O)(M)$

$T_{p13} = k_{111}(M)$

$T_{p14} = k_{135}(N) + k_{136}(NO) + k_{139}(N_2) + k_{138}(NO_2)$

$T_{p15} = k_{151}(NO)$

$T_{p16} = k_{146}(NO)$

$T_{p17} = k_{118}(M)$

$T_{p18} = k_{129}(NO)$

$T_{p19} = k_{115}(M)$

$T_{p20} = k_{117}(N_2)(M)$

$T_{p21} = k_{125}(M)$

$T_{p22} = k_{122}(H_2O)(M)$

Table A-1. (Continued).

$T_{p23} = k_{124}(H_2O)(M)$

$T_{p24} = k_{110}(H_2O)(M)$

$T_{p25} = k_{140}(N_2)(M)$

$T_{p26} = k_{144}(H_2O)$

$T_{p27} = k_{105}(M)$

$T_{p28} = k_{101}(M)$

$T_{p29} = k_{103}(M)$

$T_{p30} = k_{120}(HO) + k_{121}(HO_2)$

$T_{p31} = k_{145}(H_2O)$

$T_{p32} = k_{107}(M)$

$T_{p33} = k_{100}(H_2O)(M)$

$T_{p34} = k_{104}(H_2O)$

$T_{p35} = k_{105A}(H_2O)$

$T_{p36} = k_{102}(N_2)(M)$

$T_{p37} = k_{137}(NO_2)$

$T_{p38} = k_{152}(NO_2)$

$T_{p39} = k_{114}(CO_2)(M)$

$T_{p40} = k_{127}(CO_2)$

$T_{p41} = k_{116}(H_2O)(M)$

$T_{p42} = k_{128}(H_2O)$

$T_{p43} = k_{123}(M)$

$T_{p44} = k_{119}(H_2O)$

Table A-2. Negative ion transfer coefficients.

T_{n1}	$= D_{s1,2}$[1]
T_{n2}	$= k_{225}(M) + D_{s1,4}$
T_{n3}	$= k_{234}(O)$
T_{n4}	$= k_{203}(O)$
T_{n5}	$= D_{s1,9}$
T_{n6}	$= D_{s1,10}$
T_{n7}	$= k_{221}(N) + k_{223}(O)$
T_{n8}	$= D_{s2,6}$
T_{n9}	$= k_{238}(NO)$
T_{n10}	$= k_{206}(NO)$
T_{n11}	$= k_{228}(NO)$
T_{n12}	$= k_{224}(O_2)(M)$
T_{n13}	$= k_{236}(O_2)$
T_{n14}	$= k_{226}(O_3)$
T_{n15}	$= k_{217}(O_2)(M) + k_{218}(O_3)$
T_{n16}	$= k_{239}(O) + k_{240}(O_3)$
T_{n17}	$= k_{208}(O_3)$
T_{n18}	$= k_{229}(O_3)$
T_{n19}	$= k_{215}(CO_2)(M)$
T_{n20}	$= k_{230}(CO_2)$
T_{n21}	$= k_{207}(O)$
T_{n22}	$= D_{s6,11}$

[1] $D_{si,j}$ = photodissociation rate producing ith negative ion from jth negative ion.

Table A-2. (Continued).

$T_{n23} = k_{222}(NO_2)$

$T_{n24} = k_{216}(NO_2)$

$T_{n25} = k_{241}(NO)$

$T_{n26} = k_{231}(NO) + k_{232}(NO_2)$

$T_{n27} = k_{201}(NO)$

$T_{n28} = D_{s7,12}$

$T_{n29} = k_{233}(NO_2)$

$T_{n30} = k_{202}(NO_2)$

$T_{n31} = k_{211}(NO_2) + k_{212}(O_3)$

$T_{n32} = D_{s8,13}$

$T_{n33} = k_{219}(CO_2)(M)$

$T_{n34} = k_{235}(CO_2)$

$T_{n35} = k_{227}(CO_2)$

$T_{n36} = D_{s9,14}$

$T_{n37} = k_{220}(H_2O)(M)$

$T_{n38} = k_{237}(H_2O)$

$T_{n39} = k_{200}(H_2O)(M)$

$T_{n40} = k_{210}(NO)$

$T_{n41} = k_{204}(H_2O)(M)$

$T_{n42} = k_{214}(H_2O)(M)$

$T_{n43} = k_{214}(O_3)$

$T_{n44} = k_{209}(NO)$

$T_{n45} = k_{205}(H_2O)(M)$

produce O_2^+ and NO^+ instantaneously and are not further considered explicitly in the model. The effective O_2^+ and NO^+ production rates are computed from

$$q_e(O_2^+) = q(O_2^+) + P_1 q(N^+) + P_3 q(O^+) + P_5 q(N_2^+) \quad \text{(A-1)}$$

$$q_e(NO^+) = q(NO^+) + P_2 q(N^+) + P_4 q(O^+) + P_6 q(N_2^+) \quad \text{(A-2)}$$

where

$$P_1 = \frac{k_{112}}{k_{112} + k_{113}} \quad \text{(A-3)}$$

$$P_2 = 1 - P_1 \quad \text{(A-4)}$$

$$P_3 = \frac{k_{133}(O_2)}{k_{131}(N_2) + k_{132}(M)(N_2) + k_{133}(O_2)} \quad \text{(A-5)}$$

$$P_4 = 1 - P_3 \quad \text{(A-6)}$$

$$P_5 = \frac{k_{130}(O_2)}{k_{130}(O_2) + k_{180}(O)} \quad \text{(A-7)}$$

$$P_6 = 1 - P_5 \quad . \quad \text{(A-8)}$$

Reactions and rate coefficients are defined in Table A-3.

Electron attachment to O_2, O_3, and NO_2 produce O_2^-, O^-, and NO_2^-. The attachment rates (s^{-1}) are computed from

$$(O_2^-) \quad : \quad A_1 = k_{166}(N_2)(O_2) + k_{168}(O_2)(O_2) + k_{179}(O_2)(H_2O) \quad \text{(A-9)}$$

$$(O^-) \quad : \quad A_2 = k_{170}(O_3) + k_{178}(O) \quad \text{(A-10)}$$

$$(NO_2^-) \quad : \quad A_3 = k_{165}(NO_2) \quad . \quad \text{(A-11)}$$

APPENDIX A

Detachment processes include collisional and associative detachment from O_2^- and O^- and photodetachment from O_2^-, O^-, O_3^-, NO_2^-, and NO_3^-. The detachment rates (s^{-1}) are computed from

$$(O_2^-) \quad : D_1 = k_{167}(N_2) + k_{169}(O_2) + k_{175}(N) + k_{176}(O) + k_{177}(O_2(^1\Delta)) + D_{t1} \tag{A-12}$$

$$(O^-) \quad : D_2 = k_{171}(N) + k_{172}(NO) + k_{173}(O) + k_{174}(O_2(^1\Delta)) + D_{t2} \tag{A-13}$$

$$(O_3^-) \quad : D_5 = D_{t5} \tag{A-14}$$

$$(NO_2^-) \quad : D_7 = D_{t7} \tag{A-15}$$

$$(NO_3^-) \quad : D_8 = D_{t8}. \tag{A-16}$$

where the solar photodetachment terms D_{t1} are taken as (s^{-1}):

$$(O_2^-) \quad : D_{t1} = 0.3 \tag{A-17}$$

$$(O^-) \quad : D_{t2} = 1.4 \tag{A-18}$$

$$(O_3^-) \quad : D_{t5} = 0.08 \tag{A-19}$$

$$(NO_2^-) \quad : D_{t7} = 0.08 \tag{A-20}$$

$$(NO_3^-) \quad : D_{t8} = 0.03 \tag{A-21}$$

Very little data is available on ion-ion recombination coefficients, and the rate is assumed independent of the particular positive or negative ion. The ion-ion recombination rate coefficient is computed from

$$\alpha_i = k_{242} + k_{243}(M) \quad cm^3 s^{-1} \tag{A-22}$$

The electron-ion recombination coefficients are taken as follows ($cm^3 s^{-1}$)

$$\alpha_{d1} = k_{162} \quad (O_2^+) \tag{A-23}$$

$$\alpha_{d2} = k_{164} \quad (O_4^+ \text{ and } O_2^+(N_2)) \tag{A-24}$$

$$\alpha_{d3} = k_{163} \quad (O_2^+(W),\ H_3O^+),\ H_3O^+(W),\ H_3O^+(OH),$$

$$\text{and } H_3O^+(N_2)) \tag{A-25}$$

$$\alpha_{d4} = k_{154} \quad (H_3O^+(W)_2) \tag{A-26}$$

$$\alpha_{d5} = k_{155} \quad (H_3O^+(W)_3) \tag{A-27}$$

$$\alpha_{d10} = k_{156} \quad (H_3O^+(W)_4) \tag{A-28}$$

$$\alpha_{d6} = k_{157} \quad (NO^+) \tag{A-29}$$

$$\alpha_{d7} = k_{160} \quad (NO^+(N^2),\ NO^+(CO_2),\ \text{and } NO^+(W)) \text{ A-30)}$$

$$\alpha_{d8} = k_{158} \quad (NO^+(W)_2) \tag{A-31}$$

$$\alpha_{d9} = k_{159} \quad (NO^+(W)_3) \tag{A-32}$$

The steady-state solution is obtained by writing the differential equation for each ion species and setting the time derivative for each species concentration to zero. This results in a set of coupled, non-linear equations and iterative techniques must be used for solution. The procedure employed makes use of the fact that if the total electron and ion concentrations are known, the distribution of ions (the ratio of one ion concentration to another) can be found algebraically. If the ion distributions are known, effective *lumped parameter* reaction rate coefficients can be defined to solve for the total ion concentrations as follows:

$$\alpha_d = \sum_i \alpha_{di}(M^+)_i/(M^+)_T \tag{A-33}$$

$$D = \sum_i D_i(M^-)_i/(M^-)_T \tag{A-34}$$

$$A = \sum_i A_i \tag{A-35}$$

where α_{di} are the various electron-ion recombination rates (Equations A-23 through A-32), D_i are the various detachment rates (Equations A-12 through A-16), A_i are the various attachment rates (Equations A-9 through A-11), $(M^+)_i$ is the concentration of a particular, positive ion, $(M^+)_T$ is the total positive ion concentration, and $(M^-)_i$ and $(M^-)_T$ are particular and total negative ion concentrations, respectively. The effective ion-ion recombination rate α_i has been assumed independent of the particular ions (Equation A-22). With the effective rates, the lumped parameter solutions are

$$(M^+)_T = \sqrt{q/\alpha} \tag{A-36}$$

$$(e) = \frac{q + D(M^+)_T}{A + D + \alpha_d(M^+)_T} \tag{A-37}$$

$$(M^-)_T = (M^+)_T - (e) \tag{A-38}$$

where α is obtained from the cubic equation

$$= \frac{A\alpha_i + D\alpha_d + \alpha_i\alpha_d\sqrt{q/\alpha}}{A + D + \alpha_i\sqrt{q/\alpha}} \tag{A-39}$$

and q is the total ion production rate. Thus, in the iterative procedure, the ion concentration ratios are calculated from the total electron and ion concentrations, effective lumped parameter reaction rates are defined from the ion concentration ratios, and the total electron and ion concentrations are computed from the effective rates.

The iteration converges rapidly because the ion ratios are relatively insensitive to the total electron and ion concentrations. The expressions for the ion ratios are quite complex and will not be presented here.

The following reactions and reaction rate coefficients are employed in the chemistry model. The coefficients A, B, and C are given for the reaction rate formula

$$k = A\left(\frac{T}{300}\right)^{B} e^{-C/T} \quad ,$$

where T is the air temperature (k).

Table A-3. Reactions and rate coefficients.

Reactions	Rate Coefficients A	B	C
Neutral Species Reactions			
1 $O_3 + h\nu \rightarrow O_2 + O$	(Effective values computed within model)		
2 $O_3 + h\nu \rightarrow O_2(^1\Delta) + O$			
3 $O_2 + h\nu \rightarrow O + O$			
4 $NO_2 + h\nu \rightarrow NO + O$			
* 5 $N(^2D) + O_2 \rightarrow NO + O$	7.5(-12)	+0.5	
6 $O_2(^1\Delta) \rightarrow O_2 + h\nu$	2.6(- 4)		

Table A-3. (Continued).

	Reactions	Rate Coefficients A	B	C
	Neutral Species Reactions			
* 7	$O_2(^1\Delta) + N \rightarrow O_2 + N$	2.0(-14)		600
* 8	$O_2(^1\Delta) + N_2 \rightarrow O_2 + N_2$	0		
* 9	$O_2(^1\Delta) + O \rightarrow O_2 + O$	0		
10	$O_2(^1\Delta) + O_2 \rightarrow O_2 + O_2$	2.2(-18)	+0.8	
11	$O_2(^1\Delta) + O_3 \rightarrow O_2 + O_2 + O$	4.5(-11)		2800
*12	$N + NO \rightarrow N_2 + O$	4.1(-11)		410
*13	$N + NO \rightarrow N_2 + O(^1\Delta)$	4.1(-11)		410
*14	$N + NO_2 \rightarrow NO + NO$	0		
*15	$N + NO_2 \rightarrow N_2O + O$	2.0(-11)		800
16	$N + O \rightarrow NO$	1.5(-17)		
17	$N + O + M \rightarrow NO + M$	1.0(-32)	-0.5	
18	$N + O_2 \rightarrow NO + O$	3.3(-12)	+1.0	3150
*19	$N + O_3 \rightarrow NO + O_2$	3.1(-11)		1200
20	$NO + O \rightarrow NO_2 + h\nu$	6.6(-17)	-1.9	
*21	$NO + O + M \rightarrow NO_2 + M$	6.4(-32)	-2.0	
22	$NO + O_3 \rightarrow NO_2 + O_2$	9.0(-13)		1200
23	$NO_2 + O \rightarrow NO + O_2$	9.1(-12)		
24	$O + O_2 + M \rightarrow O_3 + M$	1.1(-34)		-510
*25	$O + O_3 \rightarrow O_2(^1\Delta) + O_2$	0		
*26	$O + O_3 \rightarrow O_2 + O_2$	1.9(-11)		2300
*27	$O + HO_2 \rightarrow H + O_2$	4.2(-11)		

Table A-3. (Continued).

Reactions	Rate Coefficients A	B	C
Neutral Species Reactions			
*28 $O + HO_2 \rightarrow OH + O_2$	8.0(-11)		500
*29 $O + H_2 \rightarrow H + OH$	9.0(-12)	+1.0	4500
*30 $OH + H_2 \rightarrow H + H_2O$	3.6(-11)		2590
*31 $OH + N \rightarrow H + NO$	5.3(-11)		
*32 $H + O_3 \rightarrow OH + O_2$	2.6(-11)		
*33 $H + O_3 \rightarrow HO_2 + O$	2.6(-11)		
*34 $OH + O_3 \rightarrow HO_2 + O_2$	1.6(-12)		1000
*35 $H + O_2 + M \rightarrow HO_2 + M$	5.5(-32)	-1.0	
*36 $H + NO_2 \rightarrow OH + NO$	5.8(-10)		740
*37 $HO_2 + NO \rightarrow OH + NO_2$	2.0(-13)		
*38 $HO_2 + O_3 \rightarrow OH + O_2 + O_2$	1.0(-13)		1250
*39 $NO + OH + M \rightarrow HNO_2 + M$	6.1(-31)	-2.0	
*40 $NO_2 + OH + M \rightarrow HNO_3 + M$	1.8(-30)	-2.0	
*41 $NO_2 + HO_2 \rightarrow HNO_2 + O_2$	3.0(-14)		
*42 $OH + HO_2 \rightarrow H_2O + O_2$	2.0(-11)		
*43 $O(^1\Delta) + H_2O \rightarrow OH + OH$	2.4(-10)		
*44 $O(^1\Delta) + N_2 \rightarrow O + N_2$	1.3(-11)		-260
*45 $O(^1\Delta) + O_2 \rightarrow O + O_2$	2.3(-11)		-170
*46 $O(^1\Delta) + H_2 \rightarrow H + OH$	1.3(-10)		
*47 $O(^1\Delta) + H_2O_2 \rightarrow OH + HO_2$	2.5(-10)		
*48 $H + HO_2 \rightarrow H_2 + O_2$	4.2(-11)		350
*49 $H + HO_2 \rightarrow H_2O + O$	8.3(-11)		500

Table A-3. (Continued).

	Reactions	Rate Coefficients A	B	C
	Positive Ion and Electron Reactions			
*100	$H_3O^+ + W + M \rightarrow H^+(W)_2 + M$	3.4(-27)	-2.0	
*101	$H^+(W)_2 + M \rightarrow H_3O^+ + W + M$	1.6(+ 1)	-2.0	18200
*102	$H_3O^+ + N_2 + M \rightarrow H_3O^+(N_2) + M$	0		
103	$H_3O^+(N_2) + M \rightarrow H_3O^+ + N_2 + M$	0		
104	$H_3O^+(OH) + W \rightarrow H^+(W)_2 + OH$	1.4(- 9)		
*105	$H_3O^+(OH) + M \rightarrow H_3O^+ + OH + M$	3.0(- 3)	-2.0	12000
105A	$H_3O^+(N_2) + H_2O \rightarrow H^+(W)_2 + N_2$	0		
106	$H^+(W)_2 + W + M \rightarrow H^+(W)_3 + M$	2.3(-27)	-2.0	
*107	$H^+(W)_3 + M \rightarrow H^+(W)_2 + W + M$	1.6(- 1)	-2.0	11300
108	$H^+(W)_3 + M + W \rightarrow H^+(W)_4 + M$	2.4(-27)	-2.0	
109	$H^+(W)_4 + M \rightarrow H^+(W)_3 + W + M$	1.0(- 1)	-2.0	8600
*110	$H^+(W)_4 + W + M \rightarrow H^+(W)_5 + M$	9.0(-28)	-2.0	
*111	$H^+(W)_5 + M \rightarrow H^+(W)_4 + W + M$	1.3(+ 0)	-2.0	7700
112	$N^+ + O_2 \rightarrow O_2^+ + N(^2D)$	2.8(-10)		
113	$N^+ + O_2 \rightarrow NO^+ + O$	2.8(-10)		
*114	$NO^+ + CO_2 + M \rightarrow NO^+(CO_2) + M$	3.0(-29)	-2.0	
*115	$NO^+(CO_2) + M \rightarrow NO^+ + CO_2 + M$	3.0(- 5)	-2.0	5600
116	$NO^+ + W + M \rightarrow NO^+(W) + M$	1.5(-28)	-2.0	
*117	$NO^+ + N_2 + M \rightarrow NO^+(N_2) + M$	2.0(-31)	-4.4	
*118	$NO^+(N_2) + M \rightarrow NO^+ + N_2 + M$	1.1(- 8)	-4.4	1900
119	$NO^+(CO_2) + W \rightarrow NO^+(W) + CO_2$	1.0(- 9)		
*120	$NO^+(W) + OH \rightarrow H_3O^+ + NO_2$	6.0(-11)		

Table A-3. (Continued).

	Reactions	Rate Coefficients A	B	C
*121	$NO^+(W) + HO_2 \rightarrow H_3O^+ + NO + O_2$	5.0(-10)		
122	$NO^+(W) + W + M \rightarrow NO^+(W)_2 + M$	1.1(-27)	-2.0	
*123	$NO^+(W)_2 + M \rightarrow NO^+(W) + W + M$	5.9(- 2)	-2.0	8700
124	$NO^+(W)_2 + W + M \rightarrow NO^+(W)_3 + M$	1.6(-27)	-2.0	
125	$NO^+(W)_3 + M \rightarrow NO^+(W)_2 + W + M$	2.2(- 2)	-2.0	7000
126	$NO^+(W)_3 + W \rightarrow H^+(W)_3 + HNO_2$	7.0(-11)		
127	$NO^+(N_2) + CO_2 \rightarrow NO^+(CO_2) + N_2$	1.0(- 9)		
128	$NO^+(N_2) + H_2O \rightarrow NO^+(W) + N_2$	1.0(- 9)		
129	$NO_2^+ + NO \rightarrow NO^+ + NO_2$	2.9(-10)		
130	$N_2^+ + O_2 \rightarrow O_2^+ + N_2$	5.0(-11)	-0.8	
131	$O^+ + N_2 \rightarrow NO^+ + N$	1.2(-12)	-1.0	
*132	$O^+ + N_2 + M \rightarrow NO^+ + N + M$	6.0(-29)	-2.0	
133	$O^+ + O_2 \rightarrow O_2^+ + O$	2.0(-11)	-0.4	
134	$O_2^+ + W + M \rightarrow O_2^+(W) + M$	2.8(-28)	-2.0	
135	$O_2^+ + N \rightarrow NO^+ + O$	1.2(-10)		
136	$O_2^+ + NO \rightarrow NO^+ + O_2$	4.5(-10)		
137	$O_2^+ + NO_2 \rightarrow NO_2^+ + O_2$	6.6(-10)		
*138	$O_2^+ + NO_2 \rightarrow NO^+ + O_3$	0		
139	$O_2^+ + N_2 \rightarrow NO^+ + NO$	1.0(-16)		
*140	$O_2^+ + N_2 + M \rightarrow O_2^+(N_2) + M$	0		
*141	$O_2^+(N_2) + M \rightarrow O_2^+ + N_2 + M$	0		
*142	$O_2^+ + O_2 + M \rightarrow O_4^+ + M$	3.9(-30)	-3.2	
*143	$O_4^+ + M \rightarrow O_4^+ + O_2 + M$	2.6(- 5)	-3.2	5400

Table A-3. (Continued).

	Reactions		Rate Coefficients A	B	C
144	$O_2^+(W) + W$	$\rightarrow H_3O^+ + OH + O_2$	2.0(-10)		
145	$O_2^+(W) + W$	$\rightarrow H_3O^+(OH) + O_2$	1.0(- 9)		
146	$O_2^+(W) + NO$	$\rightarrow NO^+ + W + O_2$	1.0(-10)		
147	$O_2^+(W) + O_2(^1\Delta)$	$\rightarrow O_2^+ + W + O_2$	1.0(-10)		
*148	$O_2^+(N_2) + O_2$	$\rightarrow O_4^+ + N_2$	0		
149	$O_4^+ + W$	$\rightarrow O_4^+(W) + O_2$	1.5(- 9)		
150	$O_2^+(W) + O_2$	$\rightarrow O_4^+ + W$	2.0(-10)		2300
151	$O_4^+ + NO$	$\rightarrow NO^+ + O_2 + O_2$	5.0(-10)		
*152	$O_4^+ + NO_2$	$\rightarrow NO_2^+ + O_2 + O_2$	0		
153	$O_4^+ + O$	$\rightarrow O_2^+ + O_3$	3.0(-10)		
154	$H^+(W)_3 + e$	$\rightarrow H + 3(W)$	5.1(- 6)		
155	$H^+(W)_4 + e$	$\rightarrow H + 4(W)$	6.1(- 6)		
156	$H^+(W)_5 + e$	$\rightarrow H + 5(W)$	7.4(- 6)		
157	$NO^+ + e$	$\rightarrow \frac{3}{4}N(^2D) + \frac{1}{4}N + O$	4.0(- 7)	-1.0	
158	$NO^+(W)_2 + e$	$\rightarrow NO + 2(W)$	3.0(- 6)	-0.2	
*159	$NO^+(W)_3 + e$	$\rightarrow NO + 3(W)$	5.0(- 6)	-0.2	
*160	$NO^+(N_2) + e$	$\rightarrow NO + N_2$	1.5(- 6)	-1.0	
161	$N_2^+ + e$	$\rightarrow N(^2D) + N$	2.7(- 7)		
162	$O_2^+ + e$	$\rightarrow O(^1\Delta) + O$	2.1(- 7)	-0.7	
163	$O_2^+(W) + e$	$\rightarrow O_2 + W$	1.5(- 6)	-0.7	
*164	$O_4^+ + e$	$\rightarrow O_2 + O_2$	1.5(- 6)	-0.7	
165	$e + NO_2$	$\rightarrow NO_2^-$	4.0(-11)		

Table A-3. (Continued).

	Reactions		Rate Coefficients A	B	C
166	$e + O_2 + N_2$	$\rightarrow O_2^- + N_2$	1.0(-31)		
167	$O_2^- + N_2$	$\rightarrow e + O_2 + N_2$	1.9(-12)	+1.5	4990
168	$e + O_2 + O_2$	$\rightarrow O_2^- + O_2$	1.4(-29)	-1.0	600
169	$O_2^- + O_2$	$\rightarrow e + O_2 + O_2$	1.9(-10)	+0.5	5600
170	$e + O_3$	$\rightarrow O^- + O_2$	9.0(-12)	+1.5	
171	$O^- + N$	$\rightarrow e + NO$	2.0(-10)		
*172	$O^- + NO$	$\rightarrow e + NO_2$	2.5(-10)	-0.8	
173	$O^- + O$	$\rightarrow e + O_2$	2.0(-10)		
174	$O^- + O_2(^1\Delta)$	$\rightarrow e + O_3$	3.0(-10)		
175	$O_2^- + N$	$\rightarrow e + NO_2$	3.0(-10)		
*176	$O_2^- + O$	$\rightarrow e + O_3$	1.5(-10)		
177	$O_2^- + O_2(^1\Delta)$	$\rightarrow e + O_2 + O_2$	2.0(-10)		
178	$O + e$	$\rightarrow O^- + h\nu$	1.3(-15)		
179	$e + O_2 + H_2O$	$\rightarrow O_2^- + H_2O$	1.4(-29)		
Negative Ion Reactions					
*200	$CO_3^- + W + M$	$\rightarrow CO_3^-(W) + M$	0		
*201	$CO_3^- + NO$	$\rightarrow NO_2^- + CO_2$	1.8(-11)	-0.5	
*202	$CO_3^- + NO_2$	$\rightarrow NO_3^- + CO_2$	2.0(-10)		
203	$CO_3^- + O$	$\rightarrow O_2^- + CO_2$	1.1(-10)		
*204	$CO_3^-(W) + NO$	$\rightarrow NO_2^-(W) + CO_2$	0		
*205	$CO_4^- + W + M$	$\rightarrow CO_4^-(W) + M$	0		
206	$CO_4^- + NO$	$\rightarrow NO_3^- + CO_2$	4.8(-11)		

Table A-3. (Continued).

	Reactions	Rate Coefficients A	B	C
207	$CO_4^- + O \rightarrow CO_3^- + O_2$	1.5(-10)		
208	$CO_4^- + O_3 \rightarrow O_3^- + CO_2 + O_2$	1.3(-10)		
*209	$CO_4^-(W) + NO \rightarrow NO_3^-(W) + CO_2$	0		
*210	$NO_2^- + W + M \rightarrow NO_2^-(W) + M$	0		
211	$NO_2^- + NO_2 \rightarrow NO_3^- + NO$	0		
212	$NO_2^- + O_3 \rightarrow NO_3^- + O_2$	1.8(-11)		
*213	$NO_2^-(W) + O_3 \rightarrow NO_3^-(W) + O_2$	0		
*214	$NO_3^- + W + M \rightarrow NO_3^-(W) + M$	0		
215	$O^- + CO_2 + M \rightarrow CO_3^- + M$	3.1(-28)	-1.0	
216	$O^- + NO_2 \rightarrow NO_2^- + O$	1.2(-9)		
217	$O^- + O_2 + M \rightarrow O_3^- + M$	1.1(-30)	-1.0	
218	$O^- + O_3 \rightarrow O_3^- + O$	5.3(-10)		
219	$O_2^- + CO_2 + M \rightarrow CO_4^- + M$	2.0(-29)	-1.0	
*220	$O_2^- + W + M \rightarrow O_2^-(W) + M$	0		
221	$O_2^- + N \rightarrow O^- + NO$	1.0(-10)		
222	$O_2^- + NO_2 \rightarrow NO_2^- + O_2$	8.0(-10)		
*223	$O_2^- + O \rightarrow O^- + O_2$	1.5(-10)		
224	$O_2^- + O_2 + M \rightarrow O_4^- + M$	3.5(-31)	-1.0	
*225	$O_4^- + M \rightarrow O_2^- + O_2 + M$	2.0(-5)	-1.0	6300
226	$O_2^- + O_3 \rightarrow O_3^- + O_2$	4.0(-10)		
*227	$O_2^-(W) + CO_2 \rightarrow CO_4^- + W$	0		
*228	$O_2^-(W) + NO \rightarrow NO_3^- + H_2O$	0		

Table A-3. (Continued).

	Reactions		Rate Coefficients A	B	C
*229	$O_2^-(W) + O_3$	$\rightarrow O_3^- + W + O_2$	0		
230	$O_3^- + CO_2$	$\rightarrow CO_3^- + O_2$	5.5(-10)	-0.5	
231	$O_3^- + NO$	$\rightarrow NO_2^- + O_2$	1.0(-11)		
232	$O_3^- + NO_2$	$\rightarrow NO_2^- + O_3$	0		
*233	$O_3^- + NO_2$	$\rightarrow NO_3^- + O_2$	2.8(-10)		
*234	$O_3^- + O$	$\rightarrow O_2^- + O_2$	2.5(-10)		
235	$O_4^- + CO_2$	$\rightarrow CO_4^- + O_2$	4.3(-10)		
*236	$CO_4^- + O_2$	$\rightarrow O_4^- + CO_2$	8.4(-12)		3000
*237	$O_4^- + W$	$\rightarrow O_2^-(W) + O_2$	0		
238	$O_4^- + NO$	$\rightarrow NO_3^- + O_2$	2.5(-10)		
239	$O_4^- + O$	$\rightarrow O_3^- + O_2$	4.0(-10)		
*240	$O_4^- + O_3$	$\rightarrow O_3^- + O_2 + O_2$	3.0(-10)		
241	$NO_3^- + NO$	$\rightarrow NO_2^- + NO_2$	1.5(-11)		
242	$M^+ + M^-$	$\rightarrow$ Products	6.0(-8)		
243	$M^+ + M^- + M$	$\rightarrow$ Products	5.6(-26)	-1.5	

APPENDIX B
IONOSPHERIC SOURCE FUNCTIONS

For sensitivity analyses, we require natural ionization source function models that incorporate the various physical relationships explicitly. We therefore want to avoid models for *effective* source functions that are derived from observed ionization or propagation conditions. We have taken models based on those in Reference B-1, since they are computationally simple and incorporate most of the desired physical relationships. We have modified the functional form in some cases to make explicit certain relationships.

GALACTIC COSMIC RAY IONIZATION

The ion production rate from galactic cosmic rays is computed from

$$q_c = 4(30 + 250\, f_c \sin^4\theta) \times 10^{-20}(M) \quad cm^{-3}s^{-1} \tag{B-1}$$

where

θ = geomagnetic latitude

(M) = total neutral particle concentration at deposition point (cm^{-3})

$$f_c = 4 - 3S \tag{B-2}$$

S = relative solar activity (0 to 1).

One measure of solar activity is the sunspot number S_{SN}, which varies from about 10 for minimum conditions to about 110 for maximum conditions. So the relative parameter S may be defined

$$S = (S_{SN} - 10)/100 \quad . \tag{B-3}$$

Reference B-1. Knapp, W.S., et al, *Reaction Rate, Collision Frequency and Ambient Ionosphere Models for Use in Studies of Radio Propagation in a Nuclear Environment*, 66TMP-18 (DASA 1765), General Electric Company—TEMPO, March 1966.

Note that the cosmic ray ion production rate varies about a factor of 4 with solar activity, and that it varies in an inverse manner with maximum ion production during minimum solar activity. The strong latitude dependence results from deflection of the charged particles by the earth's magnetic field. The given expression is applicable only to altitudes above 40 km, but as will be shown later, there is negligible HF signal absorption below this altitude.

SOLAR LYMAN-ALPHA IONIZATION

The ionization of nitric oxide (NO) due to solar Lyman-α flux is given by

$$q_{L\alpha}(NO^+) = 6.0 \times 10^{-7}(NO) f_{L\alpha} \exp\left[-1.0 \times 10^{-20} I_{02}\right] \qquad \text{(B-4)}$$

where

(NO) = nitric oxide concentration at deposition point (cm^{-3})

$$f_{L\alpha} = \frac{1}{2}(1 + S) \qquad \text{(B-5)}$$

I_{02} = line integral of (O_2) along the path of the solar flux (cm^{-2}).

If we take 21 percent of the air mass as (O_2), and employ hydrostatic equilibrium, the line integral may be computed from

$$I_{02} = 4.7 \times 10^{18} P \sec\chi \quad cm^{-2} \qquad \text{(B-6)}$$

P = atmospheric pressure at deposition point (dyne cm^{-2})

χ = solar zenith angle.

The form $\sec\chi$ is a flat earth approximation and will overestimate I_{02} (underestimate $q_{L\alpha}$) for solar zenith angles greater than about 80 degrees. The relative solar activity S is from Equation B-3.

SOLAR X-RAY IONIZATION

Solar x-rays include that part of the solar spectrum in the 0-20Å wavelength band, in which the energy transport is typically described in terms of mass absorption coefficient. The ion production rate is given by

$$q_\chi = \beta\rho \int_0^{20} F_S(\lambda)\mu_m(\lambda)\ \exp[-\mu_m(\lambda)m]\ d\lambda \qquad \text{(B-7)}$$

where

β = number of ion pairs per unit absorbed energy (1.8×10^{10} erg^{-1})

ρ = air mass density at deposition point (g cm^{-3})

λ = photon wavelength (Å)

$F_S'(\lambda)$ = solar spectrum: flux at top of atmosphere (erg cm^{-2}s^{-1}Å^{-1})

$\mu_m(\lambda)$ = mass absorption coefficient for air (cm^{2}g^{-1})

m = air mass penetrated to deposition point (g cm^{-2}) .

The integral has been computed in Reference B-1 using analytic expressions to fit the solar spectrum and mass absorption coefficients. The integral is performed piecewise due to natural breaks in the analytic curve fits and also because the solar intensity variation over the solar cycle is a function of wavelength. For λ = 0 - 8Å, the solar intensity is assumed to vary by a factor of 1000; for λ = 8 - 20Å, the variation is about a factor of 45. The results of integration produce a function of air mass penetrated (m):

$$q_x = \rho f_{1x}[I_1(m) + I_2(m)] + \rho f_{2x} I_3(m) \qquad \text{(B-8)}$$

where

$$f_{1x} = 0.001 + 0.999\ S \qquad \text{(B-9)}$$

$$f_{2x} = 0.022 + 0.978\ S \qquad \text{(B-10)}$$

and S is defined in Equation B-3. If we take hydrostatic equilibrium:

$$m = \frac{P}{g} \sec\chi \quad \text{g cm}^{-2} \qquad \text{(B-11)}$$

and the absorption integrals may be expressed as functions of P secχ. These are shown in Figure B-1, and for computational purposes are fit by the following expressions:

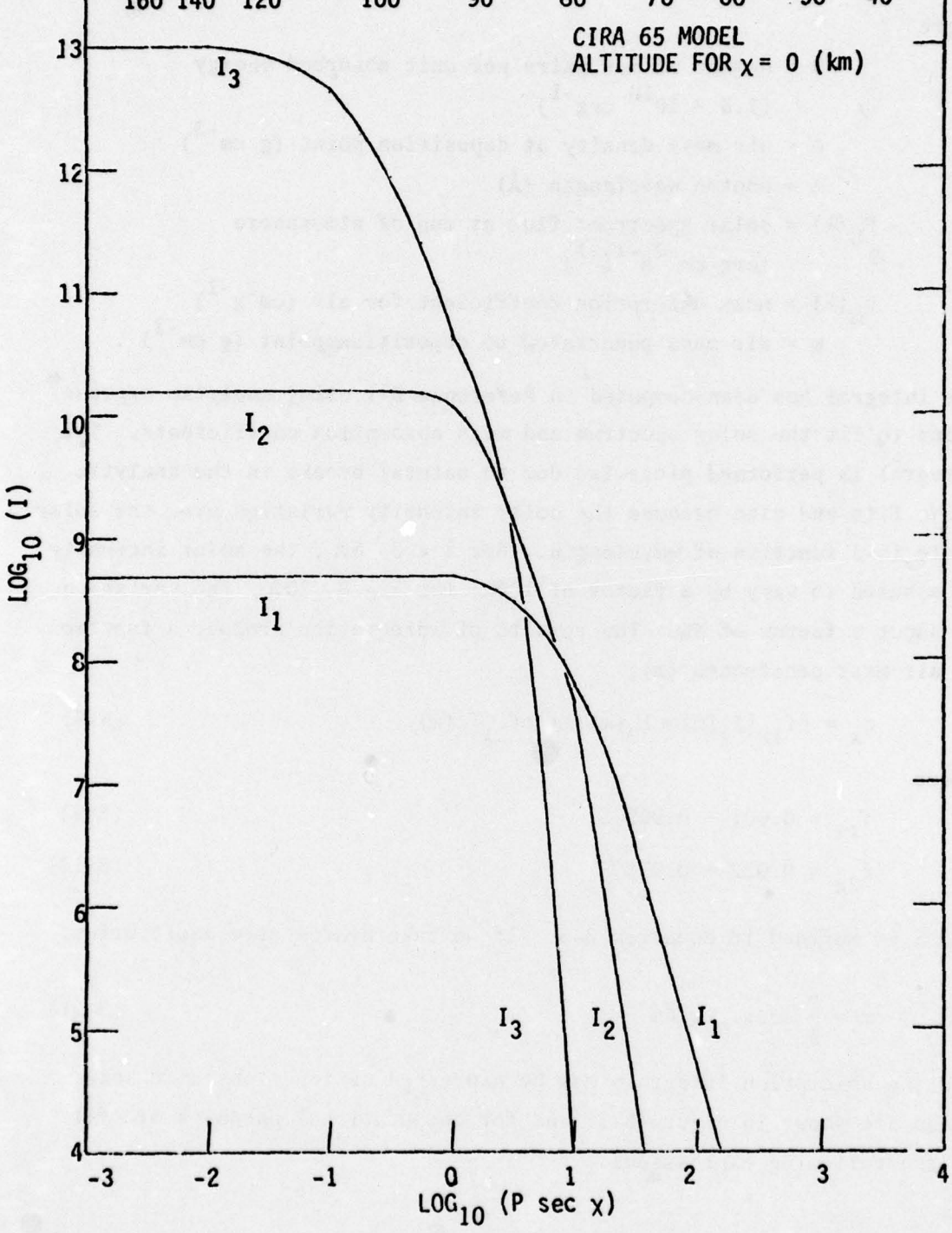

Figure B-1. X-ray absorption integrals for solar flux.

$$
\begin{aligned}
I_1(x) &= 4.80 \times 10^8 && , \quad x \le 1 \\
&= 6.04 \times 10^8 \exp(-0.23x) && , \quad 1 < x \le 10 \\
&= 2.71 \times 10^8 \exp(-0.15x) && , \quad 10 < x \le 30 \\
&= 3.89 \times 10^{11}/x^{3.46} && , \quad 30 < x
\end{aligned} \tag{B-12}
$$

$$
\begin{aligned}
I_2(x) &= 1.56 \times 10^{10} && , \quad x \le 0.1 \\
&= 4.47 \times 10^{10}/(2.871 + x^3) && , \quad 0.1 < x \le 10 \\
&= 1.20 \times 10^{14}/x^{6.43} && , \quad 10 < x
\end{aligned} \tag{B-13}
$$

$$
\begin{aligned}
I_3(x) &= 1.00 \times 10^{13} \\
&= 1.09 \times 10^{13} \exp(-8.70x) && , \quad 0.001 < x \le 0.1 \\
&= 5.40 \times 10^{11} \exp(-2.60x)/x, && 0.1 < x \le 1 \\
&= 2.40 \times 10^{11} \exp(-1.80x) && , \quad 1 < x
\end{aligned} \tag{B-14}
$$

where

$$x = P \sec\chi$$

SOLAR SOFT X-RAY AND UV IONIZATION

The first-order ionization of (O^+), (O^+), and (N_2^+) due to soft x-rays and ultraviolet energy is computed from

$$q_{UV}(O^+) = (O)\int \sigma'_O(\lambda)\, F_S(\lambda)\, \exp[-\tau_{O2}(\lambda) - \tau_{N2}(\lambda)]d\lambda \tag{B-15}$$

$$q_{UV}(O_2^+) = (O_2)\int \sigma'_{O2}(\lambda)\, F_S(\lambda)\, \exp[-\tau_{O2}(\lambda) - \tau_{N2}(\lambda)]d\lambda \tag{B-16}$$

$$q_{UV}(N_2^+) = (N_2)\int \sigma'_{N2}(\lambda)\, F_S(\lambda)\, \exp[-\tau_{O2}(\lambda) - \tau_{N2}(\lambda)]d\lambda \tag{B-17}$$

where

(O) = atomic oxygen concentration (cm^{-3})

(O_2) = molecular oxygen concentration (cm^{-3})

(N_2) = molecular nitrogen concentration (cm^{-3})

$\sigma'_O(\lambda)$ = ionization cross section for O (cm^2)

$\sigma'_{O2}(\lambda)$ = ionization cross section for O_2 (cm^2)

$\sigma'_{N2}(\lambda)$ = ionization cross section for N_2 (cm^2)

$F_S(\lambda)$ = solar photon flux spectrum at top of atmosphere (photons $cm^{-2}\ S^{-1}\mathring{A}^{-1}$) .

$$\tau_{O2}(\lambda) = \sigma_{O2}(\lambda)\int_z^\infty (O_2)dL \qquad \text{(B-18)}$$

$$\tau_{N2}(\lambda) = \sigma_{N2}(\lambda)\int_z^\infty (N_2)dL \qquad \text{(B-19)}$$

$\sigma_{O2}(\lambda)$ = total absorption cross section for O_2 (cm^2)

$\sigma_{N2}(\lambda)$ = total absorption cross section for N_2 (cm^2)

The line integrals defining the optical depths τ_{O2} and τ_{N2} (Equations B-18 and B-19) are along the path of solar flux down to altitude z. The ionization and absorption cross sections are quite structured, and since the photon flux spectrum is not sufficiently well established or constant, broad-band averages are employed for both the flux and cross-sections. These are listed in Table B-1. We compute the line integrals of Equations B-18 and B-19 from

$$\int_z^\infty (O_2)dL = \frac{f_{O2}P}{32\ m_o g}\sec\chi \qquad \text{(B-20)}$$

$$\int_z^\infty (N_2)dL = \frac{f_{N2}P}{28\ m_0 g}\sec\chi \qquad \text{(B-21)}$$

where f_{O2} and f_{N2} are the local volume mixing ratios for (O_2) and (N_2), respectively, and $m_0 = 1.66 \times 10^{-24}$ g . So that the integrals of Equations B-15 through B-17 may be precomputed as a function of a single variable, we make the following approximations for the volume mixing ratios

Table B-1. Ionization and absorption cross sections (units of 10^{-18} cm^2) and free space solar fluxes from 10 to 1026 Å.

λ(Å)	$10^{-9}\varphi_0\lambda$	$\sigma'(O)$	$\sigma'(O_2)$	$\sigma'(N_2)$	$\sigma(O_2)$	$\sigma(N_2)$
1025.7	26		1.0		1.7	
1000-1027	15		1.3		1.8	
989.8	5		1.8		2.2	0.4
977.0	30		3		3.7	0.8
972.5	10		25		30	280
949.7	5		5		5.6	1.9
911-1000	37		9		11	10
850-911	95	3	9		11	12
796-850	25	3.5	18		22	10
700-796	50	5	25	21	30	26
600-700	47	10	25	26	30	33
584.3	29	13	25	24	30	30
500-600	30	15	25	20	30	25
400-500	24	11	25	20	30	25
303.8	43	10	15	9	17	10
300-400	29	10	15	12	16	15
230-300	31	9	13	8	15	9
170-230	33	7	10	5	11	6
110-170	3.5	2.8	5	1.8	5	1.8
80-110	2.4	1.1	2	0.5	2	0.5
60-80	1.8	0.5	1	0.25	1	0.25
30-60	1.5	0.25	0.5	0.12	0.5	0.12
20-30	0.12	0.06	0.1	1.0	0.1	1.0
10-20	0.02	0.30	0.6	0.3	0.6	0.3

$$f_{O2} = 0.21 \quad , \quad P \geq 1.65$$
$$= 0.21 - 0.017 \ln (1.65/P) \quad , \quad P < 1.65 \qquad \text{(B-22)}$$

$$f_{N2} = 0.79 \quad , \quad P \geq 1.65$$
$$= 0.79 - 0.012 \ln (1.65/P) \quad , \quad P < 1.65 \qquad \text{(B-23)}$$

The ion production rates are then given by

$$q_{UV}(O^+) = \rho f_0 f_{UV} I_4(P \sin\chi) \qquad \text{(B-24)}$$

$$q_{UV}(O^+) = \rho f_{UV} I_5(P \sin\chi) \qquad \text{(B-25)}$$

$$q_{UV}(N_2^+) = \rho f_{UV} I_6(P \sin\chi) \qquad \text{(B-26)}$$

where f_0 is the volume mixing ratio to atomic oxygen and

$$f_{UV} = \frac{1}{2}(1 + S) \quad , \qquad \text{(B-27)}$$

and the relative solar activity S is from Equation B-3. The functions I_4, I_5, and I_6 are illustrated in Figure B-2. For computational purposes, we employ the following curve-fit expressions:

$$I_4(X) = 2.94 \times 10^{14} \exp(-129X)/X^{0.432} \quad , \quad x \leq 0.0316$$
$$= 3.20 \times 10^{7} \exp(+28.7X)/X^{3.63} \quad , \quad 0.0316 < x \leq 0.1$$
$$= 9.23 \times 10^{11} \exp(-7.47X)/X^{0.741} \quad , \quad 0.1 < x \qquad \text{(B-28)}$$

$$I_5(X) = 1.24 \times 10^{15} \exp(-198X) \quad , \quad x \leq 0.01$$
$$= 6.16 \times 10^{10} \exp(+14.6X)/X^{1.69} \quad , \quad 0.01 < x \leq 0.1$$
$$= 2.63 \times 10^{13} \exp(-7.04x) \quad , \quad 0.1 < x \quad . \qquad \text{(B-29)}$$

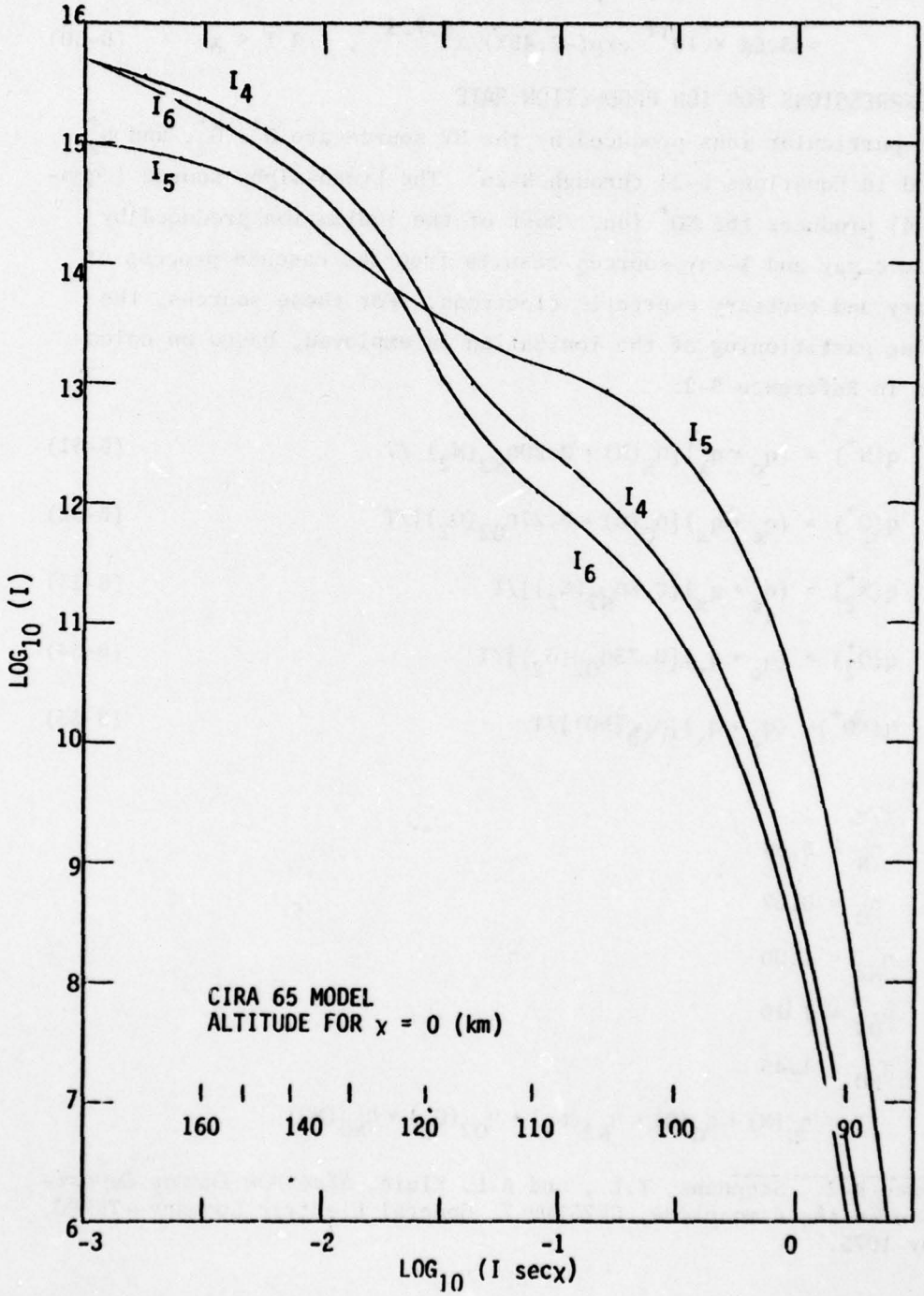

Figure B-2. Soft x-ray and UV absorption integrals for solar flux.

$$I_6(X) = 5.70 \times 10^{13} \exp(-126X)/X^{0.667} \quad , \quad x \leq 0.0316$$

$$= 1.36 \times 10^{7} \exp(+25.9X)/X^{3.69} \quad , \quad 0.0316 < x \leq 0.1$$

$$= 3.54 \times 10^{11} \exp(-7.45X)/X^{0.723} \quad , \quad 0.1 < x \qquad \text{(B-30)}$$

FINAL EXPRESSIONS FOR ION PRODUCTION RATE

The particular ions produced by the UV source are O^+, O_2^+, and N_2^+, as noted in Equations B-24 through B-26. The Lyman-alpha source (Equation B-4) produces the NO^+ ion. Most of the ionization produced by the cosmic ray and X-ray sources results from the cascade process of secondary and tertiary energetic electrons. For these sources, the following partitioning of the ionization is employed, based on calculations in Reference B-2:

$$q(N^+) = (q_c + q_x)[\eta_N(N) + 0.20\eta_{N2}(N_2)\ /T \qquad \text{(B-31)}$$

$$q(O^+) = (q_c + q_x)[\eta_O(O) + 0.27\eta_{O2}(O_2)]/T \qquad \text{(B-32)}$$

$$q(N_2^+) = (q_c + q_x)[0.8\eta_{N2}(N_2)]/T \qquad \text{(B-33)}$$

$$q(O_2^+) = (q_c + q_x)[0.73\eta_{O2}(O_2)]/T \qquad \text{(B-34)}$$

$$q(NO^+) = (q_c + q_x)[\eta_{NO}(NO)]/T \qquad \text{(B-35)}$$

where

$$\eta_N = 0.54$$

$$\eta_O = 0.67$$

$$\eta_{N2} = 1.00$$

$$\eta_{O2} = 1.10$$

$$\eta_{NO} = 1.45$$

$$T = \eta_N(N) + \eta_O(O) + \eta_{N2}(N_2) + \eta_{O2}(O_2) + \eta_{NO}(NO)$$

Reference B-2. Stephens, T.L., and A.L. Klein, *Electron Energy Deposition in the Atmosphere*, GE75TMP-7, General Electric Company—TEMPO, May 1975.

Note that for typical mesospheric mixing ratios (78 percent N_2, 21 percent O_2, less than 0.1 percent O, less than one part per million NO), the ion partition of the cosmic and X-ray sources is as follows:

ION	FRACTION
N^+	.154
O^+	.063
N_2^+	.624
O_2^+	.169
NO^+	(less than about 10^{-6}).

☆U.S. GOVERNMENT PRINTING OFFICE. 1979 677-017/48